

Master Thesis

**Exploring the existence of prebiotic species:
ALMA observations of amine-containing
organic molecule in star-forming regions.**

Harumi Minamoto

17M01629

Nomura Laboratory

Department of Earth and Planetary Sciences, Tokyo Institute of Technology

January 31, 2019

Abstract

A variety of complex organic molecules have been observed for decades in the interstellar medium. Some of them are considered to be delivered to the primordial Earth by comets, and contributed to the chemical evolution leading to terrestrial life. One example of such prebiotic species is amino acid. Glycine, the simplest amino acid, has been detected in comet 81P/Wild 2 and comet 67P/Churyumov-Gerasimenko but its presence in molecular clouds is still uncertain. Detection of glycine in molecular clouds was attempted by several radio observations, but none of them succeeded.

We focused on methylamine (CH_3NH_2), which is thought to be potential interstellar precursors to glycine. It is confirmed by the experiment that the reaction of CH_3NH_2 with CO_2 in water ice yields glycine under UV irradiation. In terms of exploration in the Solar system, CH_3NH_2 is reported to exist with glycine in comets. However, a robust detection of CH_3NH_2 has been reported only in Sgr B2(N) in the case of molecular clouds.

In this work we analyzed the ALMA archival data toward 3 star-forming regions, Orion Kleinmann-Low nebula (hereafter Orion-KL), IRAS 16293-2422 (IRAS 16293), and L483.

As a result of the analysis, CH_3NH_2 was not be detected in low mass star-forming regions of IRAS 16293 and L483, but in high mass star-forming region of Orion-KL, 6 candidate emission lines were detected. CH_3NH_2 concentrates in Hot Core. In addition, we found that the average LSR velocity V_{LSR} and FWHM line width are estimated to be $4.84 \pm 0.22 \text{ km s}^{-1}$ and $4.16 \pm 0.22 \text{ km s}^{-1}$, respectively.

By using the rotation diagram method, we evaluated its tentative column density and rotational temperature to be $(5.5^{+1.6}_{-1.1}) \times 10^{14} \text{ cm}^{-2}$ and $95.4^{+15.5}_{-11.7} \text{ K}$, respectively.

The distribution and spectrum parameters (V_{LSR} and FWHM line width) of CH_3NH_2 in Orion-KL are reported for the first time. Regarding its rotational temperature and column density, we gave more strict restrictions than previous studies.

However, since contamination is not sufficiently studied, this detection is still tentative. We need further line identification including other frequency bands to constrain the rotational temperature and the column density.

Contents

Abstract	i
1 Introduction	1
1.1 Origin of life and Origin of organic materials	1
1.2 Star forming region	3
1.2.1 Orion Kleinmann-Low nebula	3
1.2.2 Low mass star-forming regions	4
1.3 Radio observation	6
1.3.1 ALMA	7
1.4 CH ₃ NH ₂ , a precursor of glycine	8
1.5 Purpose of this work	9
2 Observation data & Analysis	10
2.1 Observation data	10
2.2 Analysis	11
2.2.1 Reduction of SV data	11
2.2.2 Line identification	15
3 Results	17
3.1 Overall CH ₃ NH ₂ distribution	18
3.2 Spectra	26

4 Discussion	28
4.1 Column density and Rotation temperature	28
4.2 Suspicious lines	29
5 Conclusions	35
A CH₃NH₂ survey in low mass star-forming regions	37
A.1 IRAS 16293	37
A.1.1 Observation data	38
A.1.2 Results	38
A.2 L483	39
A.2.1 Observation data	40
A.2.2 Results	40
B Distribution of CH₃NH₂ lines contaminated by other molecular line emission in Orion-KL	43
B.1 Integrated intensity maps	43
B.2 Channel maps	48
Acknowledgments	64
References	65

Chapter 1

Introduction

1.1 Origin of life and Origin of organic materials

Life was born in "primordial soup", a warm sea containing high concentrations of organic materials synthesized by chemical evolution. But there are various hypothesis on how the soup was formed. One hypothesis has been advocated that organic molecules synthesized in outer space was brought into the earth as a mechanism that organic matter accumulated on the earth.

A variety of organic molecules have been detected in outer space, and these are presumed to be formed by surface reaction or photochemical reaction on surface of icy mantle or grain in dense nebula such as dark nebula. Solid particles eventually gather and grow, forming planetesimals and planets.

Many organic molecules including amino acids are found in meteorites. A well-studied example of exogenous delivery of organic materials would be the Murchison meteorite, which fell into Victoria, Australia, in 1969. Many authors have reported the detection of common amino acids such as glycine (the simplest amino acid; $\text{NH}_2\text{CH}_2\text{COOH}$), alanine, and glutamic acids (e.g., Engel & Nagy, 1982).

Moreover, glycine was also discovered from the comets. In 2006, NASA's Stardust spacecraft brought back samples from comet 81P/Wild 2 to the earth and Elsila et al.

(2009) claimed the detection of glycine in this comet. In addition, glycine detection was reported in comet 67P/Churyumov-Gerasimenko by Altwegg et al. (2016), which contained molecules considered as precursors of glycine (e.g., methylamine and ethylamine).

As mentioned above, these organic molecules may be synthesized in outer space and then come to the earth with cosmic dust and meteorites. Especially comets are thought to be formed far from the central star in the protoplanetary disk, and protoplanetary disk was formed by shrinking of interstellar molecular clouds. For this reason, it is inferred that the materials formed in the interstellar molecular cloud are kept in the comets. Therefore, the presence of glycine in the comets suggests that glycine and other amino acids may exist in interstellar molecular clouds.

However, a certain detection of glycine in molecular clouds has not been reported, and its origin is still unknown. Kuan et al. (2003) claimed the first detection of glycine, however, several follow-up observations denied the detection. The emission Kuan et al. thought to be glycine was concluded to be acetone (e.g., Jones et al., 2007).

1.2 Star forming region

Previous research has revealed that various organic molecules exist in the star formation regions so far. Here we introduce the celestial bodies that we focused on in this work.

1.2.1 Orion Kleinmann-Low nebula

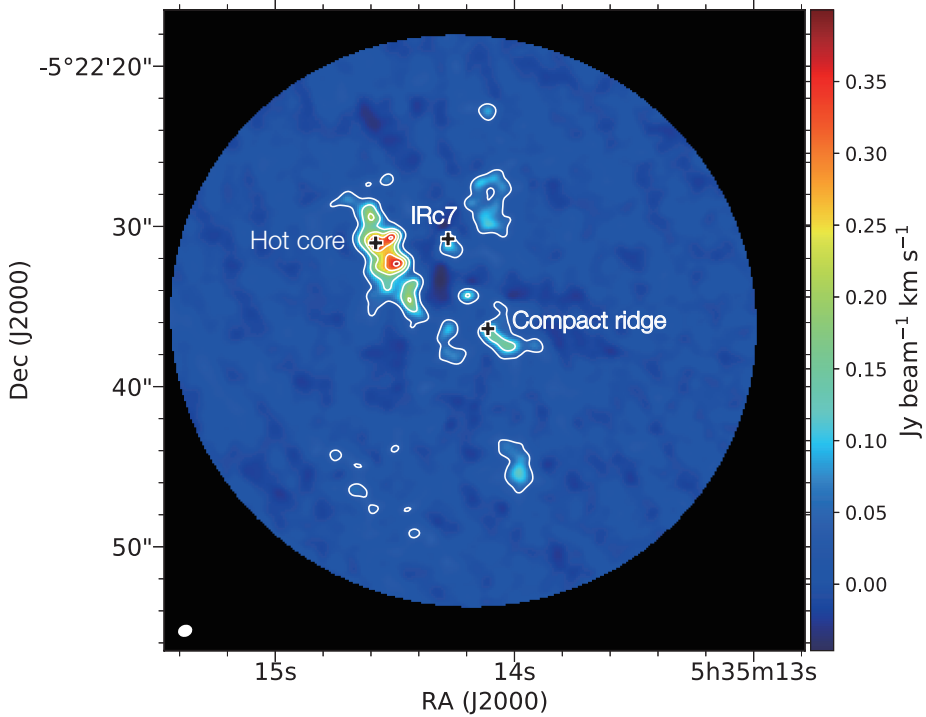


Figure 1.1: Continuum emission map for band 6 data from Hirota et al. (2015). Synthesized beam size is indicated at the bottom-left corner. The contour levels are 10 %, 30 %, 50 %, 70 %, 90 % of the peak intensity of 0.40 Jy/beam. Black crosses denote Hot core, IRc7, and Compact ridge

The Orion region hosts two well-studied star forming sites, Orion A and Orion B. Orion A is subdivided into four clouds (Orion Molecular Cloud 1-4, OMC) and OMC1 holds the Kleinmann-Low nebula (hereafter Orion-KL).

The Orion-KL is the nearest massive star-forming region, which is located approximately 418 ± 6 pc away from the sun (Kim et al., 2008). Its proximity and rich molecular composition make this region well suited for astrochemical study. Since this region was discovered in 1967 (Kleinmann & Low, 1967), numerous studies including line survey

have been conducted so far (e.g., Pagani et al., 2017; Feng et al., 2015; Gong et al., 2015; Turner, 1991).

In Orion-KL, several remarkable sources called Hot core and Compact ridge are known as regions where many organic molecules exist (Blake et al., 1987). Hot core is known as a high-density (10^6 cm^{-3}) region with a warm ($\sim 150 \text{ K}$), compact ($< 0.05 \text{ pc}$) clump (Zapata et al., 2011), and Compact ridge is also known to be a warm and dense region. Many previous studies have revealed that the chemical composition is different between these regions. While many molecules containing nitrogen (e.g., NH_3 , CH_3CN , etc.) are observed in Hot core, O-bearing species (e.g., CH_3OH , CH_3OCH_3 , etc.) are observed in Compact ridge (Favre et al., 2011).

1.2.2 Low mass star-forming regions

Chemical studies of low mass star-forming regions were relatively sparse before the 1990s. The chemical compositions of low mass star-forming regions were studied using a few abundant molecules such as NH_2 , CS , and HC_3N because molecular emission is generally weaker in low mass star-forming regions than in high mass star-forming regions. However, with the development of observation equipment, the chemical composition of low mass star-forming regions has gradually become clear.

Here, two low mass Class 0 protostars are taken as an example.

1. IRAS 16293-2422

IRAS 16293-2422 (hereafter IRAS 16293) is a deeply embedded young stellar object located in the L1689 region in the eastern part of the ρ Ophiuchus cloud (at $d = 120 \text{ pc}$ Loinard et al., 2008). It is a multiple system consisting of sources A and B, whose projected separation is $5''$ (600 au).

This object is a typical example of sources with many saturated molecules, called hot corino (Cazaux et al., 2003). Saturated COMs(Complex organic molecules; Species consisting of 6 atoms or more) such as CH_3OH , CH_3CN , HCOOCH_3 ,

$(CH_3)_2O$, C_2H_5OH , and C_2H_5CN were found (Blake et al., 1994; van Dishoeck et al., 1995; Cazaux et al., 2003).

After the start of ALMA operation, COMs survey has been actively conducted. (e.g., The ALMA Protostellar Interferometric Line Survey (PILS) Jørgensen et al., 2016)

2. L483

L483 is a dark cloud in Aquila Rift, whose distance from the Sun is 200 pc (Jørgensen et al., 2002; Rice et al., 2006). This cloud is associated with the infrared source IRAS 18148-0440, which is known to be a Class 0 protostar (Fuller et al., 1995; Chapman et al., 2013). As opposed to hot corino, carbon chain molecules (e.g., CS, CCH. See Hirota et al., 2009, 2010) are detected in this source, and recently, detection of unsaturated species such as CNCN, NCCN, and NCO has been reported by single-dish observation (Agúndez et al., 2018; Marcelino et al., 2018). In addition, saturated organic molecules such as CH_3OH , $HCOOCH_3$ and HNCO are detected as in IRAS 16293 by the high resolution observation with the interferometer (Oya et al., 2018).

1.3 Radio observation

The radio observation has been established as one method of space observations since discovery of the first cosmic radio by Karl G. Jansky in the 1930's and the world's first radio telescope made by Grote Reber. It has also made great development with the progress of radar technology during World War II. Since then, observations have been carried out at multiple wavelength (not only visible light and radio but also X-rays and infrared), and unveiling the wonders of the universe that can not be understood only by visible light. However, because of the influence of atmospheric absorption, only visible light, radio waves and part of infrared radiation are observable from the ground. In terms of radio observation, frequency below 20 MHz do not pass through the ionosphere, and at high frequencies they are easily absorbed by atmospheric oxygen and water vapor. For this reason, it is appropriate to install the radio telescope in places with high altitude and low water vapor.

The characteristics of radio observation that are not in other wavelength are as follows.

- Low energy

The temperature at which the peak of the blackbody radiation is located in the millimeter or the submillimeter wave range is about 10–50 K. Temperature of molecular cloud cores where the protostar is born is typically as low as 10 K. Therefore, we can explore the formation process of primitive star and its evolution by radio observation. And also it is possible to observe molecular emission lines existing around the cores.

- Long wavelength

Radio is hard to be absorbed by interstellar microparticles, and it is possible to observe deeply in molecular cloud cores.

- Well-established interference technology

In a telescope called an interferometer, it is possible to obtain a high resolution by

observing with multiple remote antennas and interfering radio waves.

With the above characteristics, radio observation regarded as important tool in astronomy.

1.3.1 ALMA

Atacama Large Millimeter/submillimeter Array (ALMA) is a synthetic aperture radio telescope in the Atacama desert in Chile. Atacama desert has high clear-sky ratio (low annual rainfall of 100 mm or less) and high altitude (about 5000 m), so the amount of water vapor in the sky is small. We can observe radio waves from celestial bodies without being affected by atmospheric absorption as much as possible there. Because of the wide flat ground, the antenna can be arranged in a wide range of 18.5 km, its resolution corresponds to one large telescope with the same diameter.

Although high resolution observation can be cited as an advantage of the interferometer, on the other hand, it is not very suitable for the weak line survey because of the difficulty in improving sensitivity with the sparse array. However, by combining a short baseline antenna group and a long baseline antenna group, ALMA enabled simultaneous high sensitivity and high resolution observation. It is expected that even COMs that have not been detected in the past can be found by ALMA observations.



Figure 1.2: Atacama Large Millimeter/submillimeter Array. Credit by ALMA (ESO/NAOJ/NRAO), R. Hills (ALMA)

1.4 CH₃NH₂, a precursor of glycine

Methylamine (CH₃NH₂) is considered as a precursor of the simplest amino acid glycine. Recent experimental studies have shown several reaction pathways to forming glycine in water containing ices starting from CH₃NH₂ and CO₂ subjected to high energy electrons (Holtom et al., 2005) or UV radiation (Bossa et al., 2009; Lee et al., 2009). Under similar conditions glycine can decompose to yield CH₃NH₂ and CO₂ (Ehrenfreund et al., 2001).

Interstellar CH₃NH₂ was first detected toward Sgr B2 at 3.5 cm (Fourikis et al., 1974) and at 3mm (Kaifu et al., 1974). Recently, CH₃NH₂ has been detected in cometary samples of the Stardust mission (Glavin et al., 2008) and comet 67P/C-G (Altwegg et al., 2016, 2017).

However, in molecular clouds, a robust detection of CH₃NH₂ has been reported only for Sgr B2(N) (Halfen et al., 2013) so far, while a variety of complex organic molecules have been detected by radio observations. Although tentative detection in Orion-KL reported by Pagani et al. (2017), its physical properties such as distribution and temperature are still unclear.

1.5 Purpose of this work

Since glycine has not been detected in the ISM, its precursors would be essential in searching for good candidate sources for glycine surveys. Although CH_3NH_2 is a probable precursor, its detection has been reported only for one object. Since CO_2 exists in most of molecular clouds and CH_3NH_2 is a direct precursor candidate to glycine, CH_3NH_2 -rich sources will turn into promising glycine survey targets. Such studies would also accelerate the discussion regarding the exogenous delivery of prebiotic species to planets and connection between the Universe and life. Therefore, in this study, we aim to detect CH_3NH_2 in the star-formation regions other than Sgr B2.

This paper is organized as follows. In Section 2, we present the observations and the data reduction. In Sect. 3, we report distribution maps and spectrum of several CH_3NH_2 candidate lines, and in Sect. 4 we discuss column density of CH_3NH_2 and predictable line contaminations. Conclusions are summarized in Sect. 5.

Chapter 2

Observation data & Analysis

2.1 Observation data

We analyzed 2 ALMA archival data. First we used Cycle 2 data (ADS/JAO.ALMA#2013.1.00553.S, Pagani et al. (2017)) We also employed the ALMA Science Verification (SV) data (ADS/JAO.ALMA#2011.0.00009.SV) at band 6 to fill up the missing frequency coverage of Cycle 2 data. Details of each data are summarized in Table 2.1.

Cycle 2 data cube was already calibrated by Pagani et al., and the reduced data are available on the web site of CDS (Centre de Donnees astronomiques de Strasbourg)¹. Since the SV data contained not only line emission but continuum emission, we subtracted continuum emission statistically by the method described in Section 2.2.1.

In addition, we used Common Astronomy Software Applications (CASA) software V.5.0.0 (McMullin et al., 2007) during the procedure to analyze observational data.

¹<http://cdsarc.u-strasbg.fr/viz-bin/qcat?J/A+A/604/A32>

Table 2.1: Summary of Observations

Date	Window (spw)	Frequency range (GHz)	FWHM (arcsec)	PA (degree)
20 January 2012 (SV)	0–16	213.715–246.627	1.8×1.3	-1
29–30 December 2014 (Cycle 2)	1	215.145–216.087	1.8×1.1	86
	2	216.342–217.279	1.8×1.1	84
	3	217.273–218.211	2.2×1.0	102
	4	218.204–219.141	2.2×1.0	102
	5	219.127–220.064	1.9×1.0	95
	6	219.784–220.721	1.8×1.0	95
	7	229.757–230.694	1.4×0.8	80
	8	230.699–231.636	2.1×0.9	102
	9	232.238–233.175	1.6×1.0	80
	10	233.470–234.422	1.6×0.8	90
	11	235.084–236.021	1.7×0.9	95
	12	236.267–237.206	1.6×0.9	87
	13	244.834–245.771	1.6×0.9	79
	14	245.773–246.710	1.6×0.9	79
	15	250.154–251.091	1.5×0.9	88
	16	251.079–252.016	1.3×0.8	86

2.2 Analysis

2.2.1 Reduction of SV data

With the advent of highly sensitive facilities such as ALMA, the spectral lines which were hindered by the noise level with previous telescope can now be detected. Most of these line-rich sources including hot cores are associated with detectable continuum emission. In the analysis of molecular emission lines, the determination and the subtraction of this continuum emission is an essential, but difficult task. Therefore, we improved the method devised in Sanchez-Monge et al. (2017) and deduced continuum subtraction in the observed UV domain (the raw visibilities measured by the interferometer). We introduce the method and results in this section.

Determination of the continuum level

The determination of the continuum emission level of astronomical sources observed in a spectral line observing mode is based on the identification of channels free of line emission, i.e. line-free channels.

First, we obtain the spectra for which we want to estimate the continuum level. In the case of Orion-KL, many molecular emission exist in Hot core ($\text{RA}_{J2000} : 05^{\text{h}}35^{\text{m}}14^{\text{s}}.580$, $\text{Dec}_{J2000} : -05^{\circ}22'31''.029$) or Compact ridge ($\text{RA}_{J2000} : 05^{\text{h}}35^{\text{m}}14^{\text{s}}.2775$, $\text{Dec}_{J2000} : -05^{\circ}22'30''.776$), so we extracted spectra from circular regions with a diameter of $1''$.0 with the coordinates indicated by Hirota et al. (2015) as the center. The peak of the distribution of the intensity values is determined with a Gaussian fit by assuming the Gaussian random error distribution with the mean value E and the standard deviation σ . The width is small in case of pixels with little or no line emission, but for line contaminated regions the distribution becomes broader and the exact location of the peak more uncertain. Therefore, we set the range of the Gaussian fitting from 0 to $1/3$ of the peak intensity in line contaminated side, and calculated the mean value E and the standard deviation σ (see Figure 2.1).

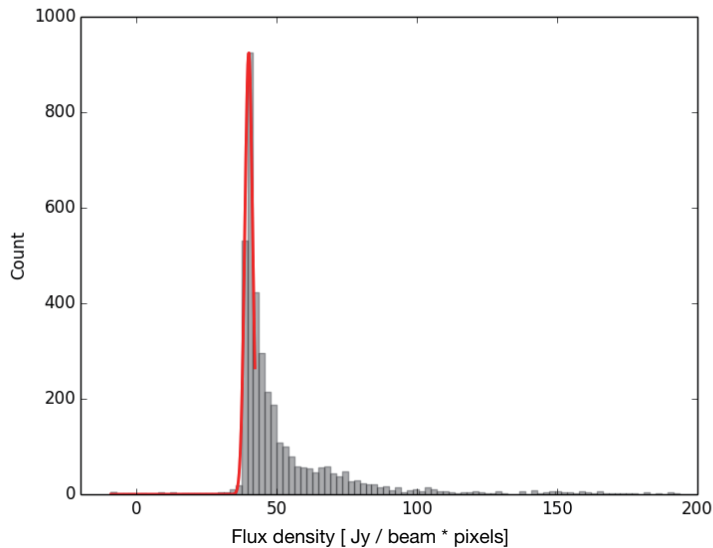


Figure 2.1: Schematic description of the process of determination of the continuum level toward Orion-KL: shown are the flux density distributions of Hot core (histogram) with the resulting fit overlaid (red line).

Imaging line cubes

Subsequently, the part of the distribution within $E - 3\sigma$ is defined as line-free channels. Hot core and Compact ridges have different spectra because of the disparate chemical composition, so we determined the line-free channels individually and subtracted the continuum in the UV domain by CASA task UVCONTSUB with channels common to the two regions. After the continuum subtraction, CASA task CLEAN was used to deconvolve the images by applying natural weighting. The synthesized beam size of each data cube is listed in Table 2.1. The velocity resolution is 0.6 km s^{-1} for Cycle 2 data and 0.7 km s^{-1} for SV data respectively.

Figure 2.2 shows examples of original and continuum-subtracted spectra towards Hot core. Since the base line defined in this analysis seems to be reasonable, the continuum subtraction has succeeded.

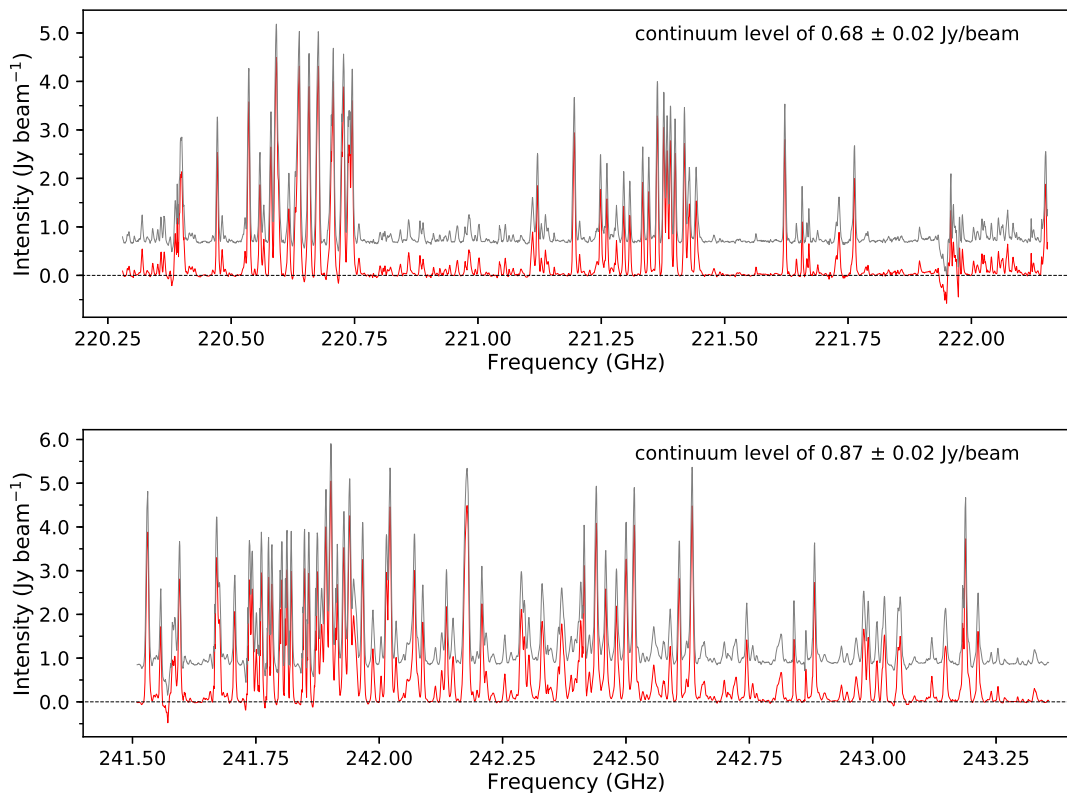


Figure 2.2: The original spectra (gray) and continuum-subtracted spectra (red) towards Hot core. The dotted line represents the base line (0 level). The continuum emission level subtracted from the original spectra, together with its uncertainty, is listed in the upper right part of each panel.

2.2.2 Line identification

Line selection and identification were carried out according to the following procedure.

1. The transition lines of CH_3NH_2 contained within the frequency coverage of the observation data were listed from the catalog. Spectroscopic data of CH_3NH_2 are provided by Motiyenko et al. (2014) and JPL Molecular Spectroscopy catalog². We considered that detection of high excitation temperature or weak line strength transition is not realistic, and set thresholds that $S\mu^2 > 25 \text{ D}^2$ and $E_u < 200 \text{ K}$. We note that line strength S , the dipole moment μ , and the upper state energy E_u . Intensity is proportional to $S\mu^2$.

In addition, using the catalog obtained from JPL database, the Cologne database for molecular spectroscopy (CDMS)³, and Splatalogue⁴'s "Hot Cores" filter, we investigated whether transitions of other species exist within $\pm 2 \text{ km s}^{-1}$ around the rest frequency of CH_3NH_2 . If other molecular emission lines exist at a distance of 2 km s^{-1} or more, they are expected to spectrally resolve with high velocity resolution (0.7 km s^{-1} for SV data, 0.6 km s^{-1} for Cycle 2).

The selection criteria of other species was set as follows; the transitions whose E_u is lower than 500 K. Transitions of CH_3NH_2 which is predicted to be blended were excluded from the survey.

As a result of the catalog selection, 24 transition were listed from 201 transitions as detection candidates.

2. In order to find regions where signals exist in common among a series of data sets, we drew integrated intensity maps using CASA task IMMOMENT. The integrated velocity range is 3.0-12.0 km s^{-1} , corresponding to typical velocity component of

²<http://spec.jpl.nasa.gov>

³<https://cdms.ph1.uni-koeln.de/cdms/portal/>

⁴<http://www.splatalogue.net/>

Hot core ($4.8\text{-}6 \text{ km s}^{-1}$) and that of Compact ridge ($7.2\text{-}9.6 \text{ km s}^{-1}$). These values were adopted from Feng et al. (2015).

3. Emission at the center of Hot core were found in most of integrated intensity maps.
4. We extracted spectrum for transitions with no line blending around $\pm 2 \text{ km s}^{-1}$ from Hot core. Here we checked again for blending. We investigated whether wider features existed in the spectrum subtracted from Hot core by eye and selected 6 lines among 24 transitions.
5. Subsequently, we estimated the systemic velocity and the line width of CH_3NH_2 by the Gaussian fitting from 6 transitions (see Section 3.2, Table 3.2).

Chapter 3

Results

The data obtained for CH₃NH₂ are summarized in Table 3.1. Here the rest frequencies, product of the line strength and the dipole moment ($S\mu^2$), the upper state energy (E_u), the quantum numbers, and noise level are listed.

Out of 24 selected transitions in our observational frequency range, 6 were probably identified and are reported in Table 3.1. The remaining 18 CH₃NH₂ transitions are blended with or masked by other spectral features, or its signal are below the noise level (See Appendix B).

Table 3.1: Observed rotational transitions of CH₃NH₂ in Orion-KL

Frequency [GHz]	$S\mu^2$ [D ²]	E_u [K]	Transition (J, K_a, Γ)	Noise [K]	Conversion (K to Jy/beam)	Comments
217.758	129.88	182.05	12, 2, $B_2 \rightarrow 12, 1, B_1$	0.034	0.847	Reported in Pagani+17
245.202	37.84	168.31	12, 1, $B_2 \rightarrow 11, 2, B_1$	0.037	0.069	Reported in Pagani+17
235.735	82.06	92.76	8, 2, $B_2 \rightarrow 8, 1, B_1$	0.081	0.073	Reported in Pagani+17
229.908	27.37	92.71	8, 2, $A_2 \rightarrow 8, 1, A_1$	0.064	0.051	
242.262	60.23	60.86	6, 2, $B_2 \rightarrow 6, 1, B_1$	0.166	0.073	SV data
244.887	49.54	48.09	5, 2, $B_1 \rightarrow 5, 1, B_2$	0.043	0.069	Reported in Pagani+17

3.1 Overall CH₃NH₂ distribution

Figure 3.1 shows the integrated intensity maps of the 6 transitions in Table 3.1 (see the procedure no.2 in section 2.2.2), and CH₃NH₂ emission appears mainly at Hot core and partially at IRc7. According to previous work (see e.g., Feng et al., 2015; Gong et al., 2015), N-bearing species tend to have similar peak at or near Hot core. CH₃NH₂ also shows the same trend.

Figure 3.2-3.7 show channel maps of expected unblended lines at 217.758 GHz, 245.202 GHz, 229.908 GHz, 235.735 GHz, 242.262 GHz, 244.887 GHz, respectively. The channel maps enable us to confirm the region where the radiations of molecules come and its velocity component.

In the integrated intensity map of 229.908 GHz line, emission come from the southern part of Hot core (Figure 3.1). Since it can be confirmed that the velocity component is different in the channel map (see Figure 3.5), this is considered to be the emission of another molecular line.

In addition, the extended emission in Hot core and the compact structure at Compact ridge are seen in the integrated intensity map of 242.262 GHz line (Figure 3.1). These are also considered to be emission from other molecule line by the channel map (Figure 3.6) and spectrum (Figure 3.8).

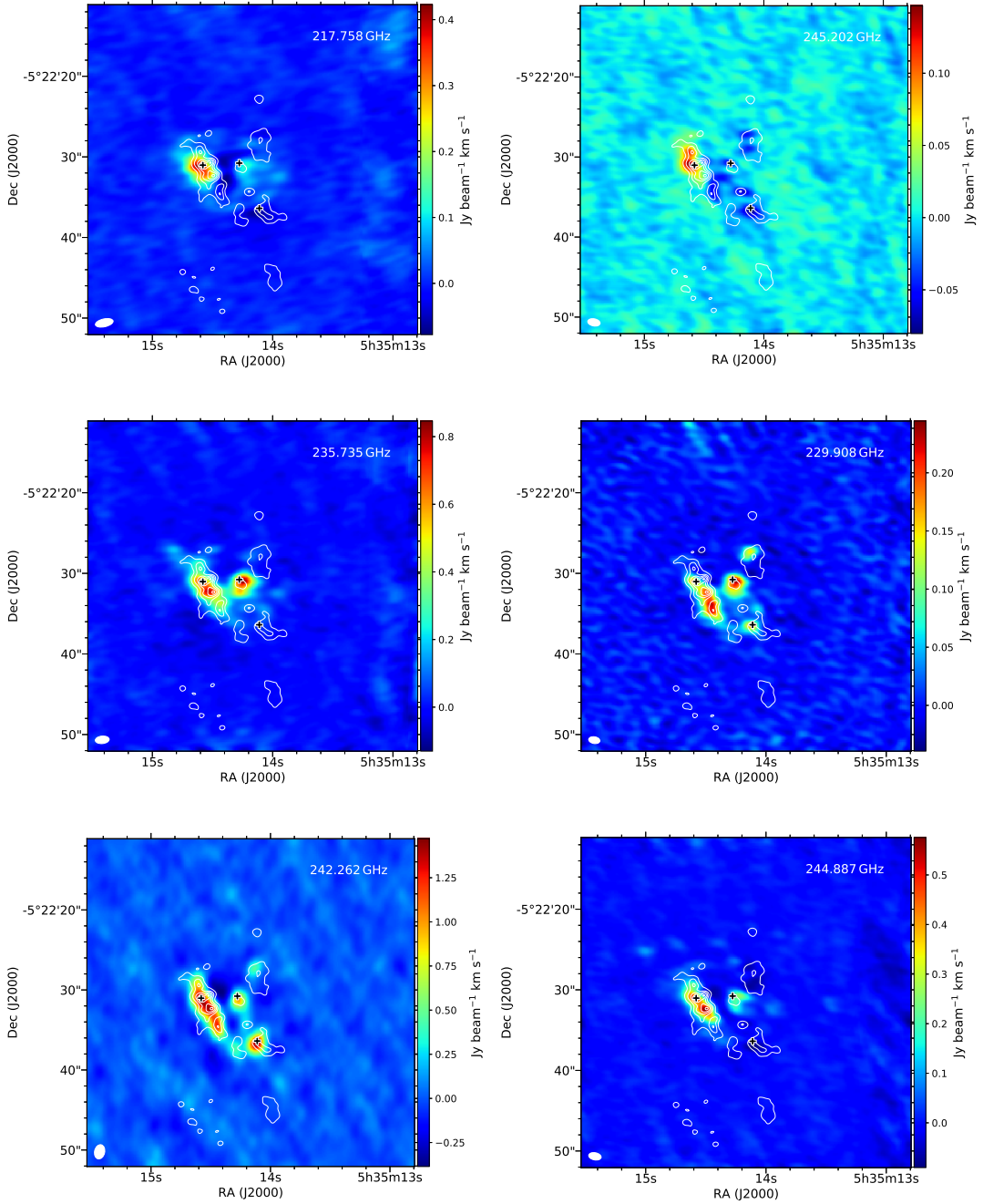


Figure 3.1: Integrated intensity maps of unblended CH_3NH_2 lines. The white contours show the 1.3 mm continuum map from Hirota et al. (2015), where the contour levels are 10 %, 30 %, 50 %, 70 %, 90 % of the peak intensity of 0.40 Jy/beam. Same as Figure 1.1 but for black crosses. The rest frequency of each transition shows in the upper right part of each panel.

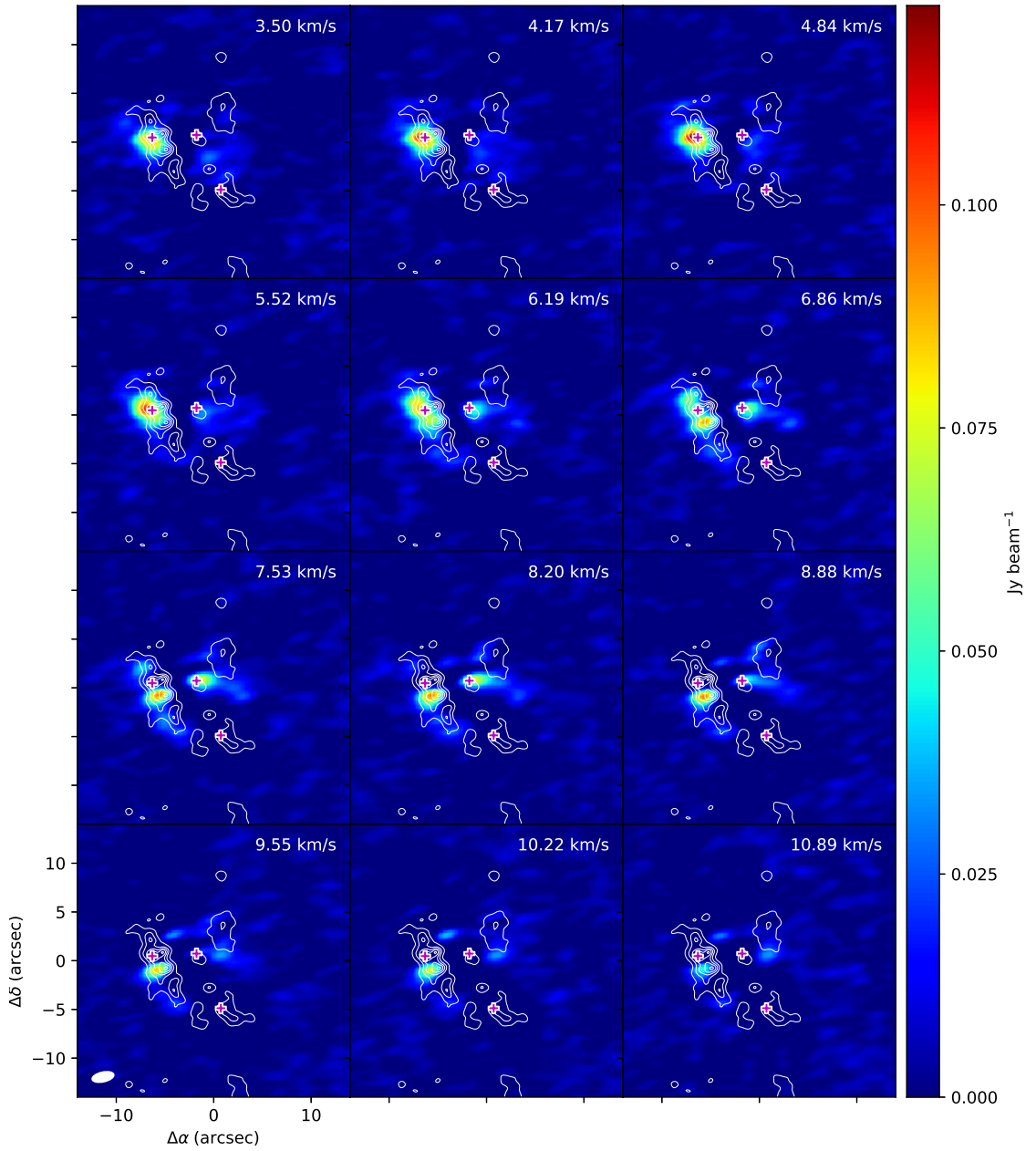


Figure 3.2: Channel map of expected unblended 217.758 GHz line show multiple velocity-dependent emission peaks: $4\text{-}6 \text{ km s}^{-1}$ towards Hot core, $7\text{-}9 \text{ km s}^{-1}$ towards IRc7. Magenta crosses denote Hot core, IRc7, and Compact ridge. Same as Figure 1.1 but for white contours.

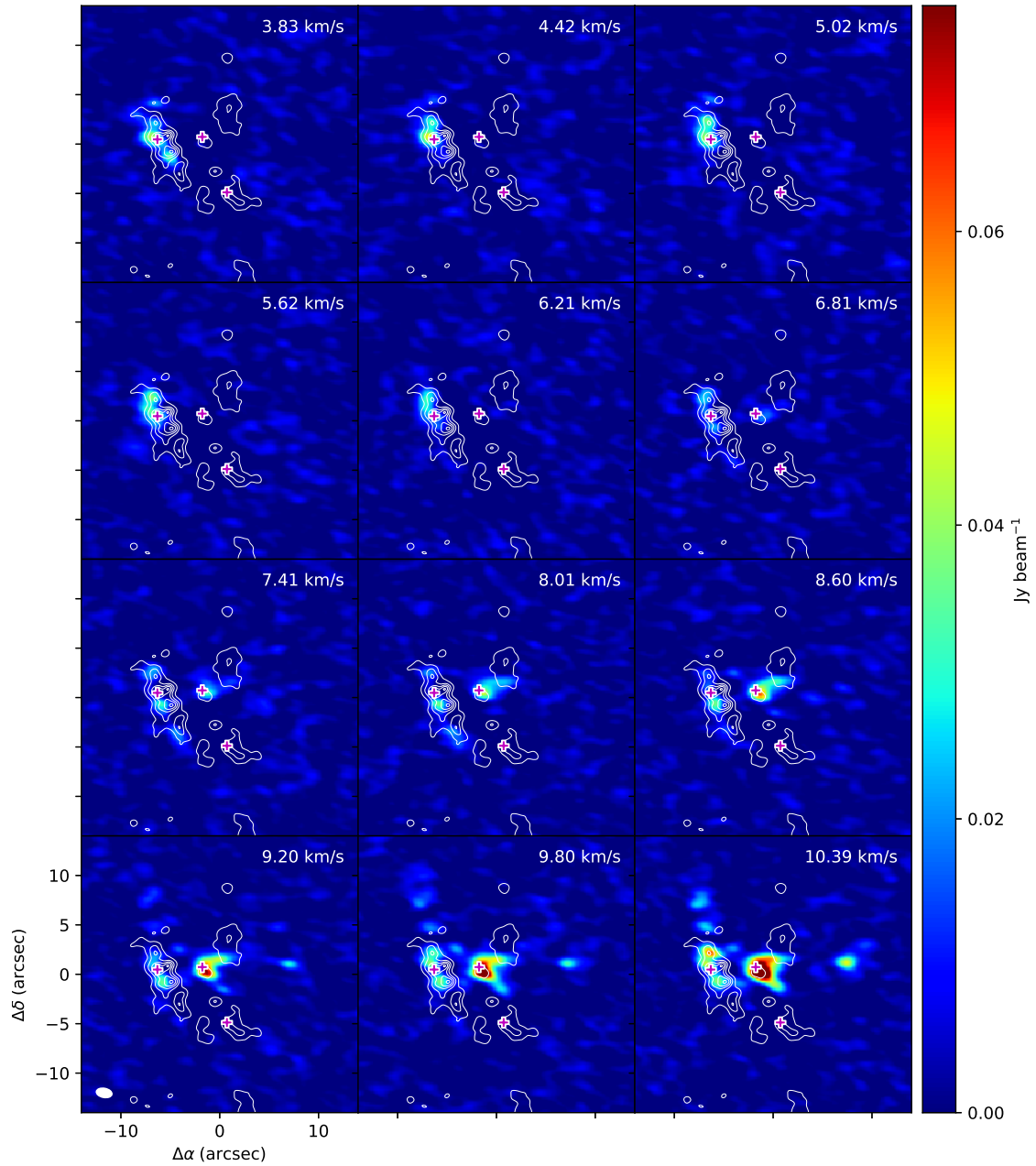


Figure 3.3: Channel map of expected unblended 245.202 GHz line.

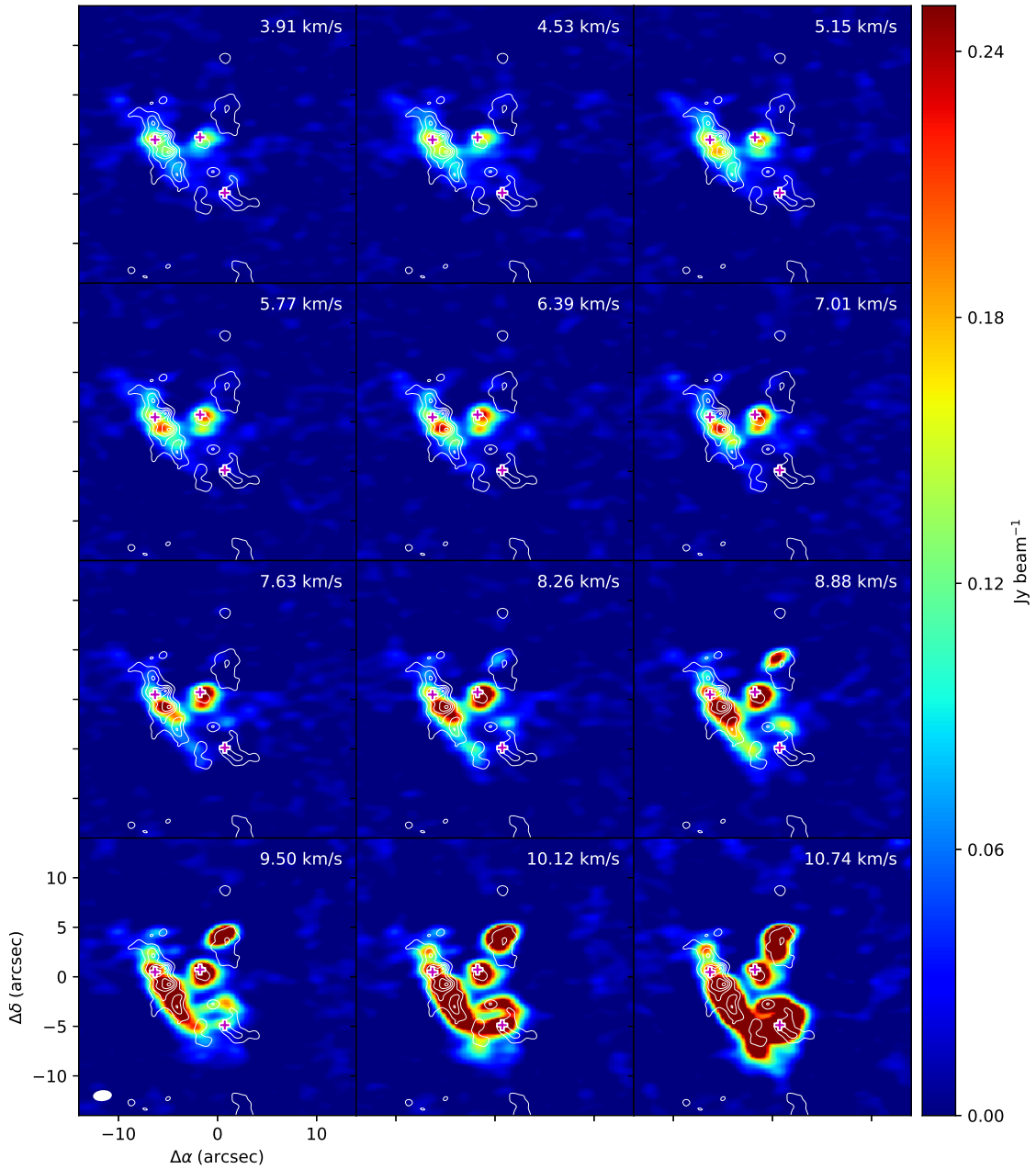


Figure 3.4: Channel map of expected unblended 235.735 GHz line.

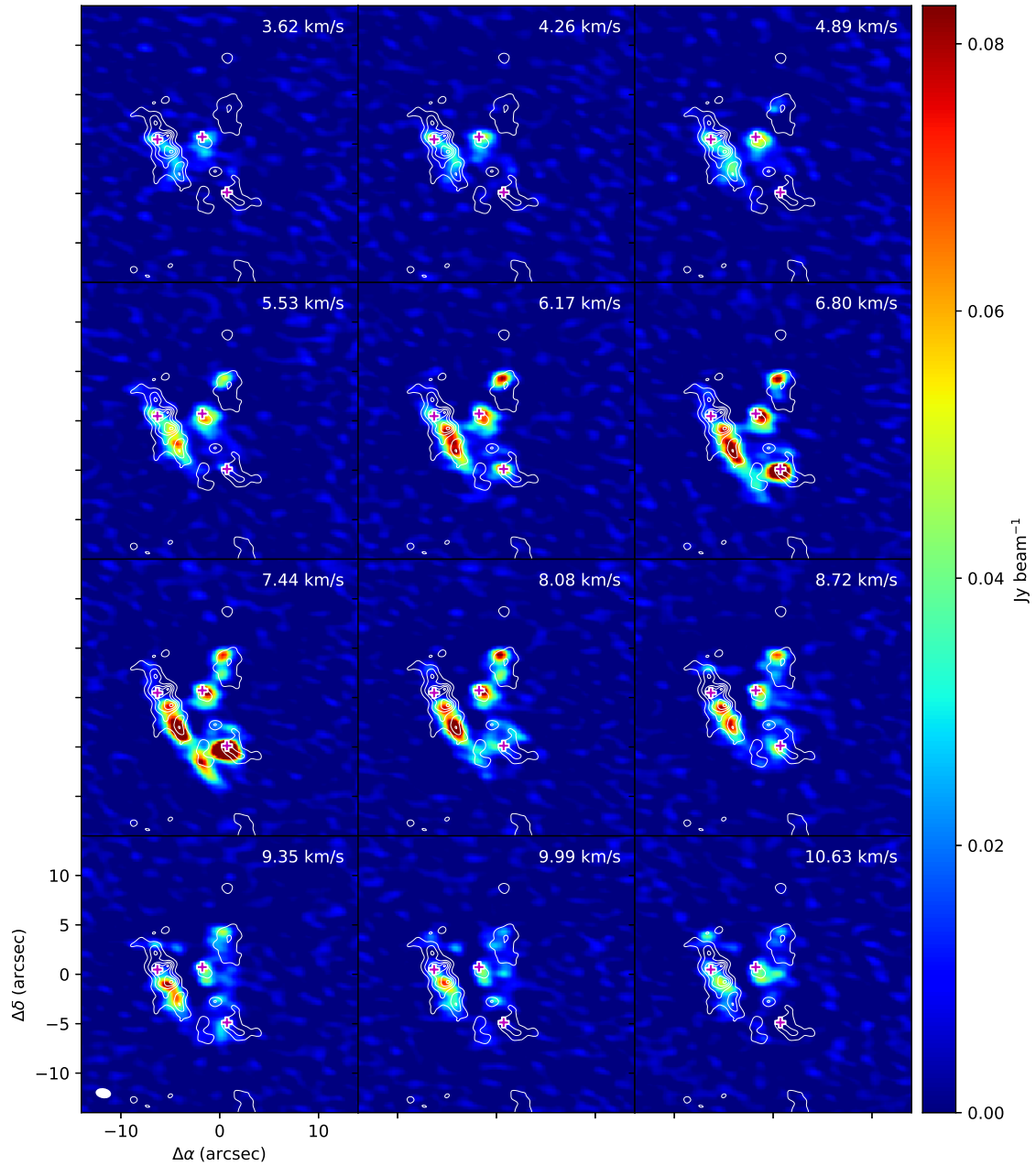


Figure 3.5: Channel map of expected unblended 229.908 GHz line.

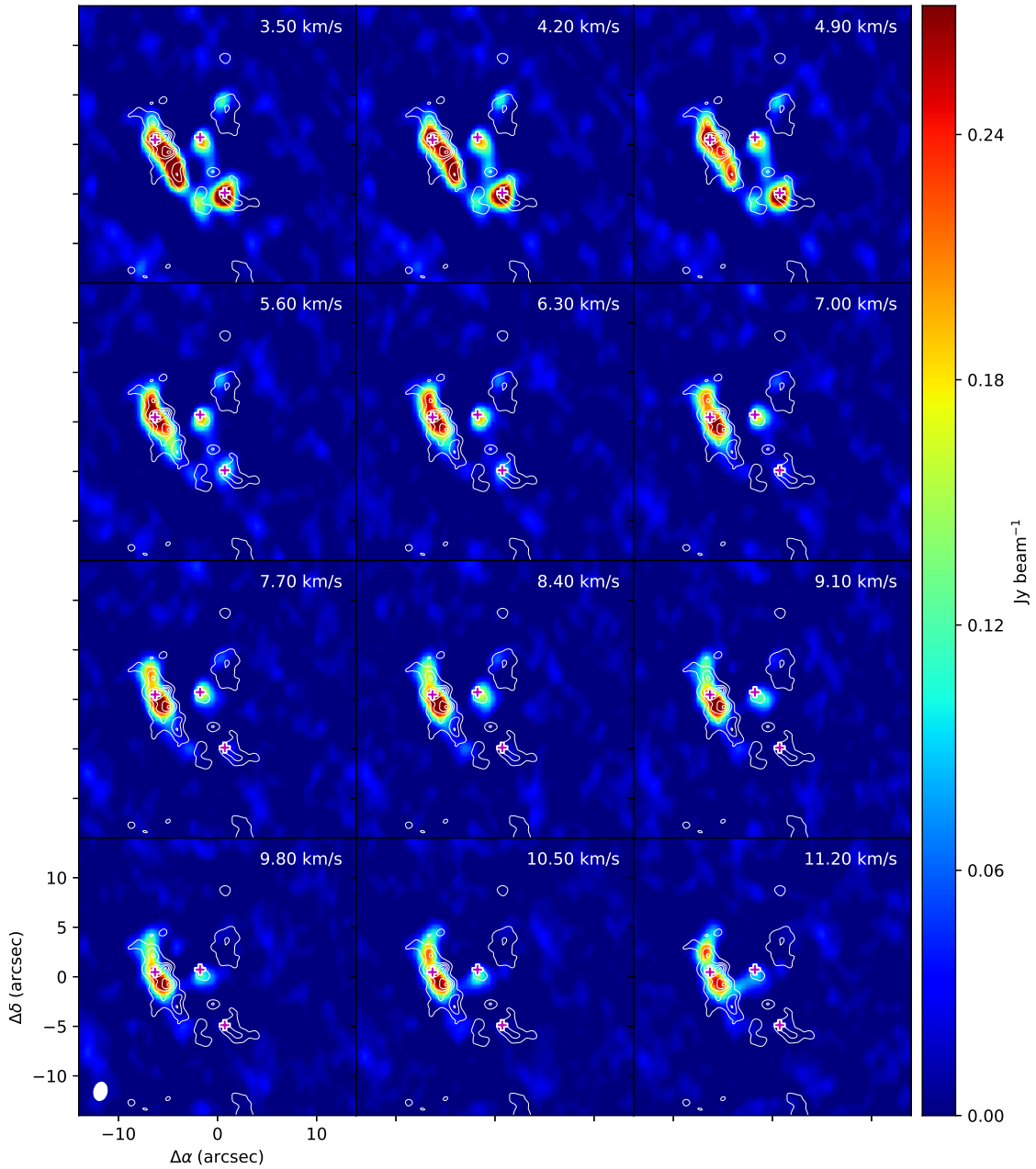


Figure 3.6: Channel map of expected unblended 242.262 GHz line.

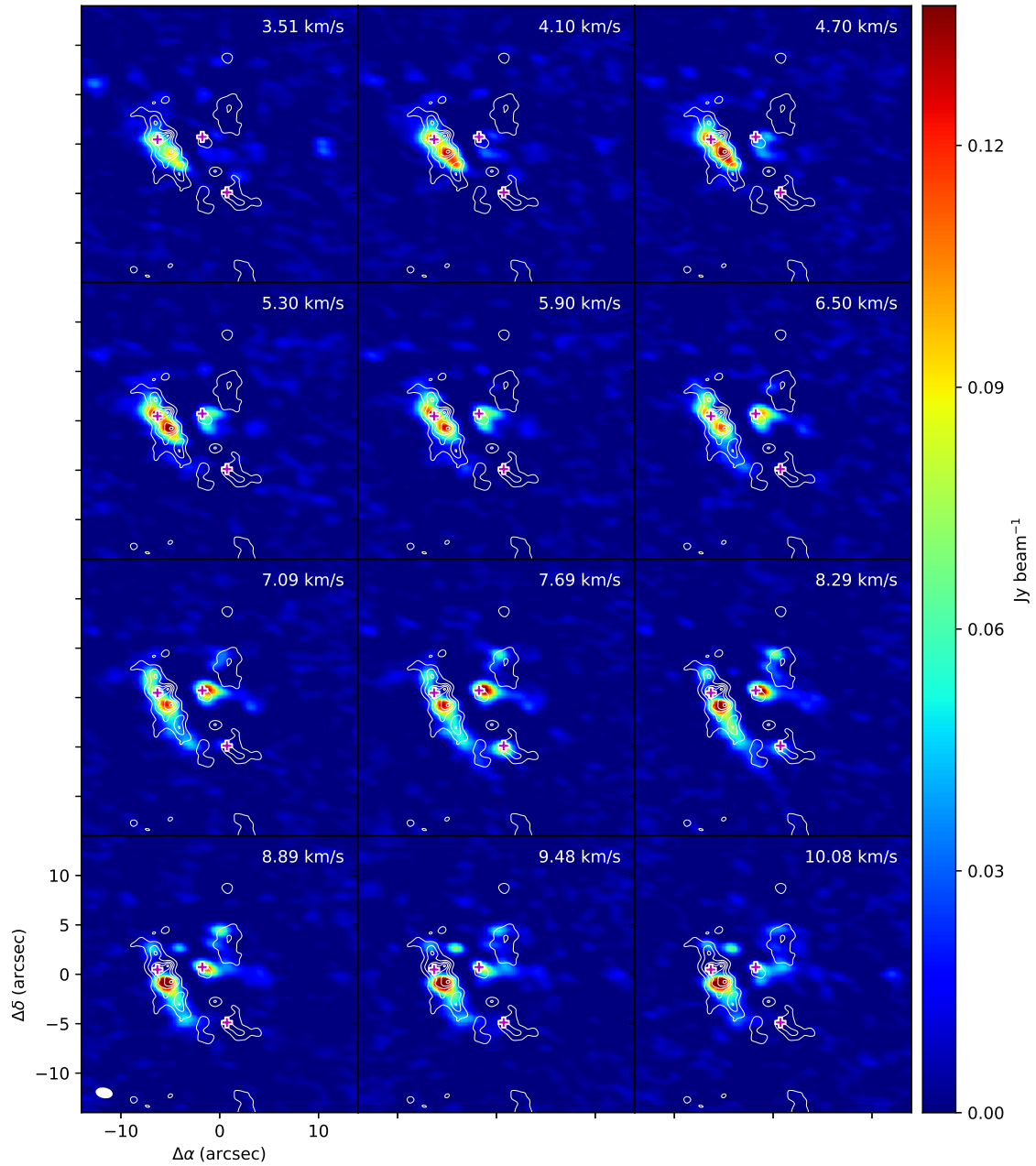


Figure 3.7: Channel map of expected unblended 244.887 GHz line.

3.2 Spectra

Figure 3.8 shows the spectra of the CH_3NH_2 lines extracted from Hot core. The spectrum were extracted from the region of $1''.0$ in diameter around Hot core ($\text{RA}_{J2000} : 05^{\text{h}}35^{\text{m}}14^{\text{s}}.580$, $\text{Dec}_{J2000} : -05^{\circ}22'31''.029$), and the Gaussian fitting was performed to obtain FWHM line widths and the mean local standard of rest velocity V_{LSR} of the emission lines. The line measurements toward Hot core are listed in Table 3.2.

The average LSR velocity and FWHM line width are estimated to be $4.84 \pm 0.22 \text{ km s}^{-1}$ and $4.16 \pm 0.79 \text{ km s}^{-1}$, respectively. V_{LSR} are consistent with those reported by Feng et al. (2015) for N-bearing COMs observed toward Hot core (e.g, 4.9 km s^{-1} for CH_2CHCN , 5.1 km s^{-1} for $\text{CH}_3\text{CH}_2\text{CN}$). On the other hand, $\Delta V_{1/2}$ of CH_3NH_2 is narrower than those of other molecule in Hot core (typically $5\text{--}15 \text{ km s}^{-1}$, Pagani et al., 2017).

Table 3.2: CH_3NH_2 line parameters toward Hot core

Frequency [GHz]	E_u [K]	peak T_B ¹ [K]	V_{LSR} ¹ [km s^{-1}]	$\Delta V_{1/2}$ ¹ [km s^{-1}]	Noise [K]	Note
217.758	182.05	0.86(0.03)	4.73(0.08)	3.99(0.24)	0.034	
245.202	168.31	0.37(0.01)	4.51(0.08)	3.86(0.33)	0.037	
229.908	92.71	0.65(0.01)	4.91(0.03)	3.19(0.06)	0.064	
235.735	92.76	1.70(0.02)	4.86(0.03)	5.60(0.10)	0.081	
242.262	60.86	2.03(0.03)	4.80(0.09)	8.04(0.23)	0.166	Partially blended
244.887	48.09	1.29(0.57)	5.23(0.90)	4.16(2.12)	0.043	

Please note that the spectrum in Figure 3.2 is superimposed with the result of the Gaussian fitting assuming the average $\Delta V_{1/2} = 4.2 \text{ km s}^{-1}$.

¹Numbers in parenthesis represent standard deviation in the unit of the last significant digits.

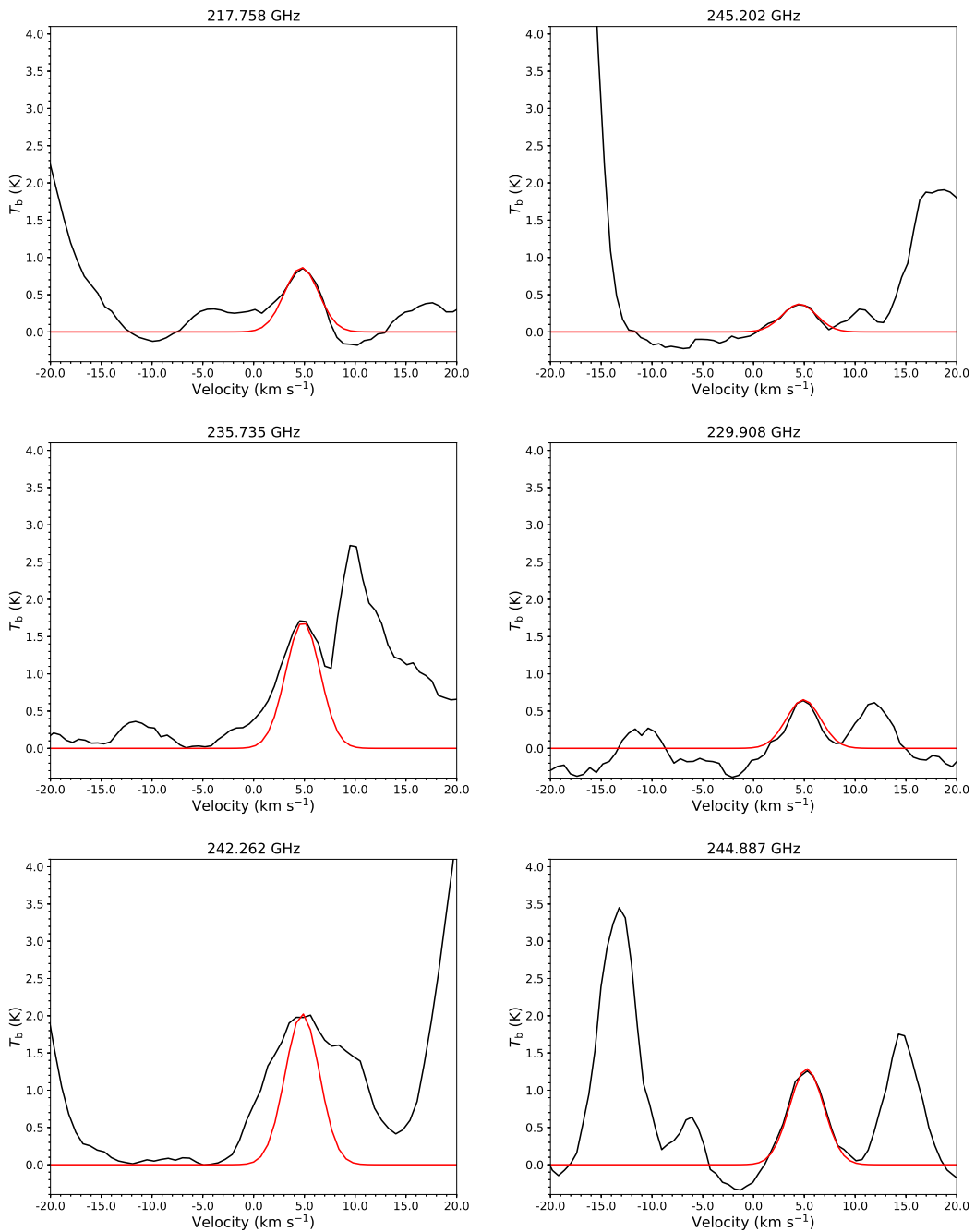


Figure 3.8: Spectrum of the CH_3NH_2 lines at each frequency observed in Hot core (black) and the result of the Gaussian fitting assuming the average $\Delta V_{1/2} = 4.2 \text{ km s}^{-1}$ (red).

Chapter 4

Discussion

4.1 Column density and Rotation temperature

In this subsection we will describe the methodologies in deriving the column density and the rotational temperature of COMs. The column density of CH₃NH₂ (N_{MA}) was estimated by using the rotational temperature diagram method, which assumes local thermodynamic equilibrium (LTE) and optically thin emission. The following equation was employed for the analysis (Turner, 1991):

$$\log \frac{3 k_{\text{B}} T_{\text{B}} \Delta V_{1/2}}{8 \pi^3 \nu S \mu_0^2} = \log \frac{N_{\text{MA}}}{U_{\text{rot}}} - \frac{E_{\text{u}} \log e}{k_{\text{B}} T_{\text{rot}}} \quad (4.1)$$

In the expression, ν is the rest frequency of the transition, μ_0 is the permanent dipole moment, U_{rot} is the rotational partition function, S is the line strength, E_{u} is the upper state energy, and T_{B} and $\Delta V_{1/2}$ are the brightness temperature and line widths (FWHM, in km s⁻¹), respectively. We assumed the average $\Delta V_{1/2} = 4.2$ km s⁻¹, which derived by the Gaussian fitting.

The brightness temperature can be converted from intensity I_{ν} when the Rayleigh-

Jeans law is applicable.

$$T_B = \frac{c^2}{2 k_B \nu^2} I_\nu \quad (4.2)$$

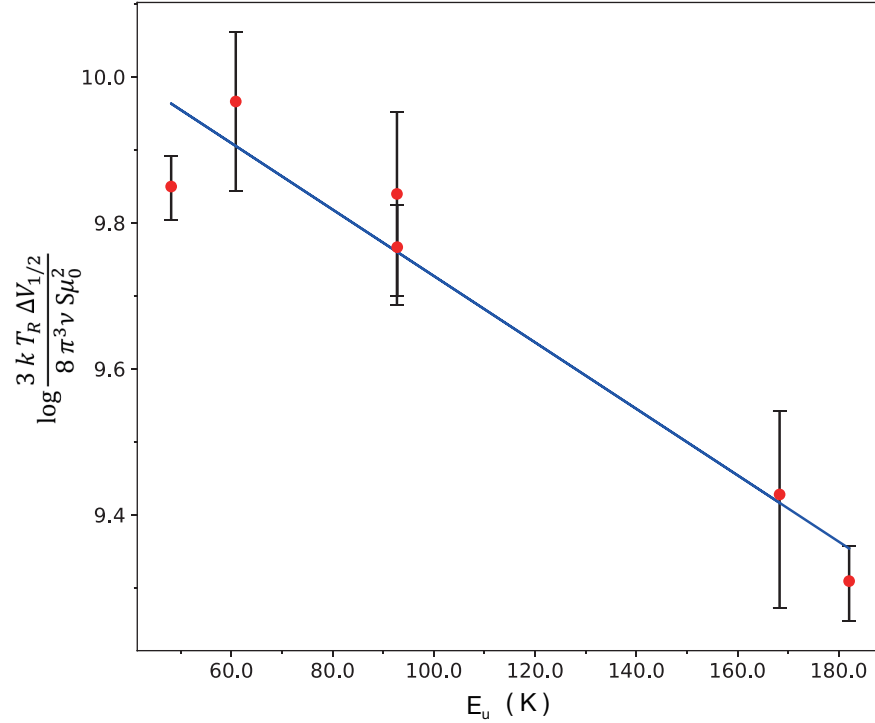


Figure 4.1: Rotation diagram of CH_3NH_2 in Hot core. The error bars represents $\pm 3 \sigma$ for each data.

The resulting plots are given in Figure 4.1. The analysis yields a rotational temperature of $T_{\text{rot}} = 95.4^{+15.5}_{-11.7}$ K, with a column density of $N_{\text{MA}} = (5.5^{+1.6}_{-1.1}) \times 10^{14}$ cm⁻².

4.2 Suspicious lines

Comparison of catalogs did not suggest contamination, but some emission lines could not be detected as CH_3NH_2 .

¹Numbers in parenthesis represent standard deviation in the unit of the last significant digits.

Table 4.1: transitions of CH_3NH_2

Frequency [GHz]	$S\mu^2$ [D ²]	E_u [K]	Transition (J, K_a, Γ)	peak T_B^{-1} [K]	V_{LSR}^{-1} [km s ⁻¹]	Noise [K]	Conversion (K to Jy beam ⁻¹)	Comments
215.670	53.92	111.48	9, 2, $E_{1-1} \rightarrow 9, 1, E_{1+1}$	3.74(0.07)	5.37(0.07)	0.043	0.077	
221.755	35.06	133.11	10, 2, $A_2 \rightarrow 10, 1, A_1$	0.33(0.03)	5.35(0.19)	0.133	0.108	SV data

As shown in Figure 4.2, the CH_3NH_2 data including 2 transitions in Table 4.1 produced point-to-point scatter perhaps because of the lower signal-to-noise ratio for the weaker transitions in SV data and possible high-level contamination.

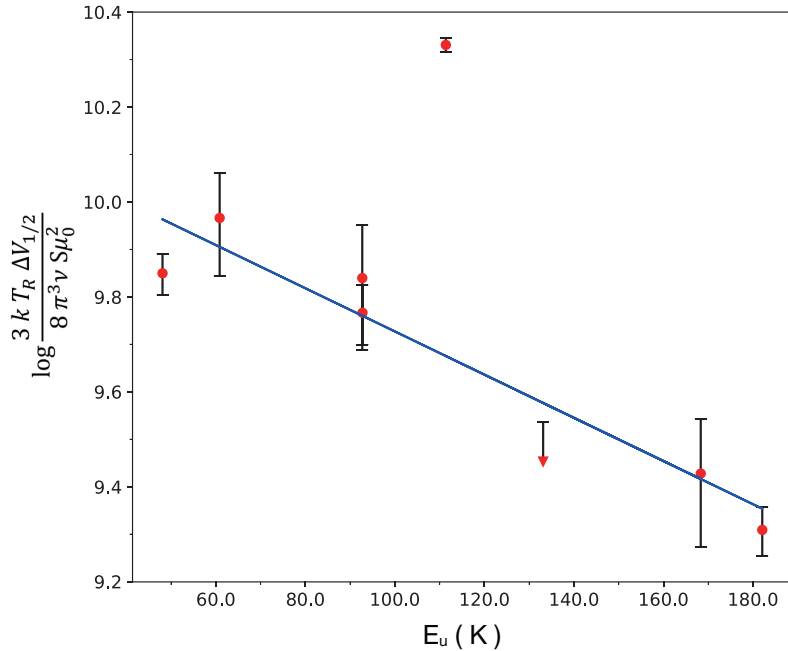


Figure 4.2: Rotation diagram of CH_3NH_2 in Hot core with additional 2 lines. The error bars on round plots represents $\pm 3\sigma$ for each data. A signal below 3σ is represented by a triangle with the error bar indicating the upper limit. The blue line is the same one as Figure 4.1.

215.670 GHz line

This emission line ($E_u = 111$ K) is seen at Hot core and IRc7 like other CH_3NH_2 transitions (see Figure 4.3 and Figure 4.5), but this line has stronger intensity than that predicted in the rotation diagram (see Figure 4.2). Since the line width is also wider than the

other CH_3NH_2 transitions (see Figure 4.3), it appears that this line is blended with other molecular emission lines existing in Hot core. Then examining the catalog including the transition of higher excitation, $\text{CH}_3\text{CH}_2\text{CN}$ (215.6687 GHz, $E_l = 604.845$ K) has come up as a candidate for blending. However, considering that T_{rot} of $\text{CH}_3\text{CH}_2\text{CN}$ in Hot core is 155 K (Feng et al., 2015), it is uncertain how much this transition of higher excitation contributes to the blending.

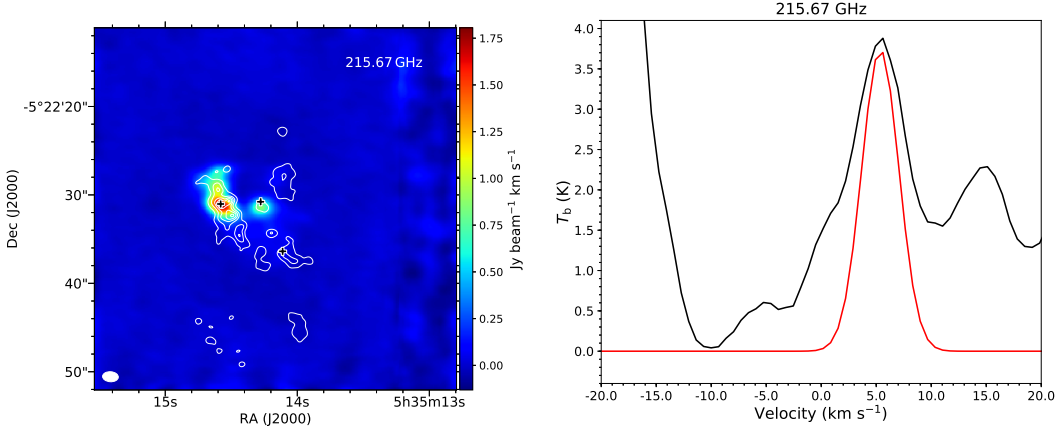


Figure 4.3: (left) Integrated intensity map of the emission for 215.670 GHz. Same as Figure 1.1 but for white contours and black crosses. (right) Spectrum of the CH_3NH_2 lines at each frequency observed in Hot core (black) and the result of the Gaussian fitting assuming the average $\Delta V_{1/2} = 4.2 \text{ km s}^{-1}$ (red)

221.755 GHz line

A faint signal was seen in Hot core in the integrated intensity map and channel maps (Figure 4.4 and 4.6). Since there was no blend of other molecular emission lines in the comparison with the catalogs, we analyzed the spectrum, but the peak intensity ($T_B = 0.33$ K) was weaker than 3σ noise level ($T_B = 0.133$ K, see Table 4.1). When we plotted this line on the rotation diagram with 3σ as the upper limit of the intensity, the derived value was consistent with other CH_3NH_2 transitions (see Figure 4.2). This emission line was included in SV data cube, so it could be possible to detect the line in future observations with higher S/N ratio.

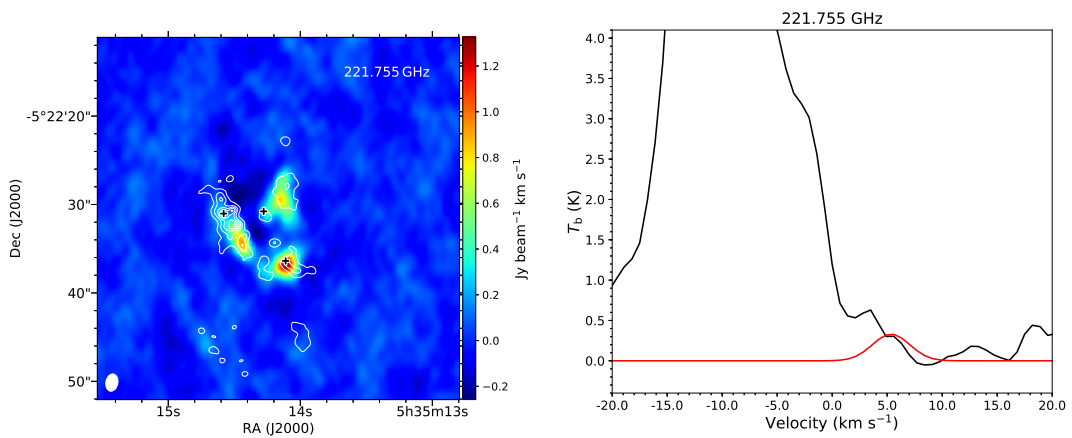


Figure 4.4: (left) Integrated intensity map of the emission for 221.755 GHz. Same as Figure 1.1 but for white contours and black crosses. (right) Spectrum of the CH_3NH_2 lines at each frequency observed in Hot core (black) and the result of the Gaussian fitting assuming the average $\Delta V_{1/2} = 4.2 \text{ km s}^{-1}$ (red)

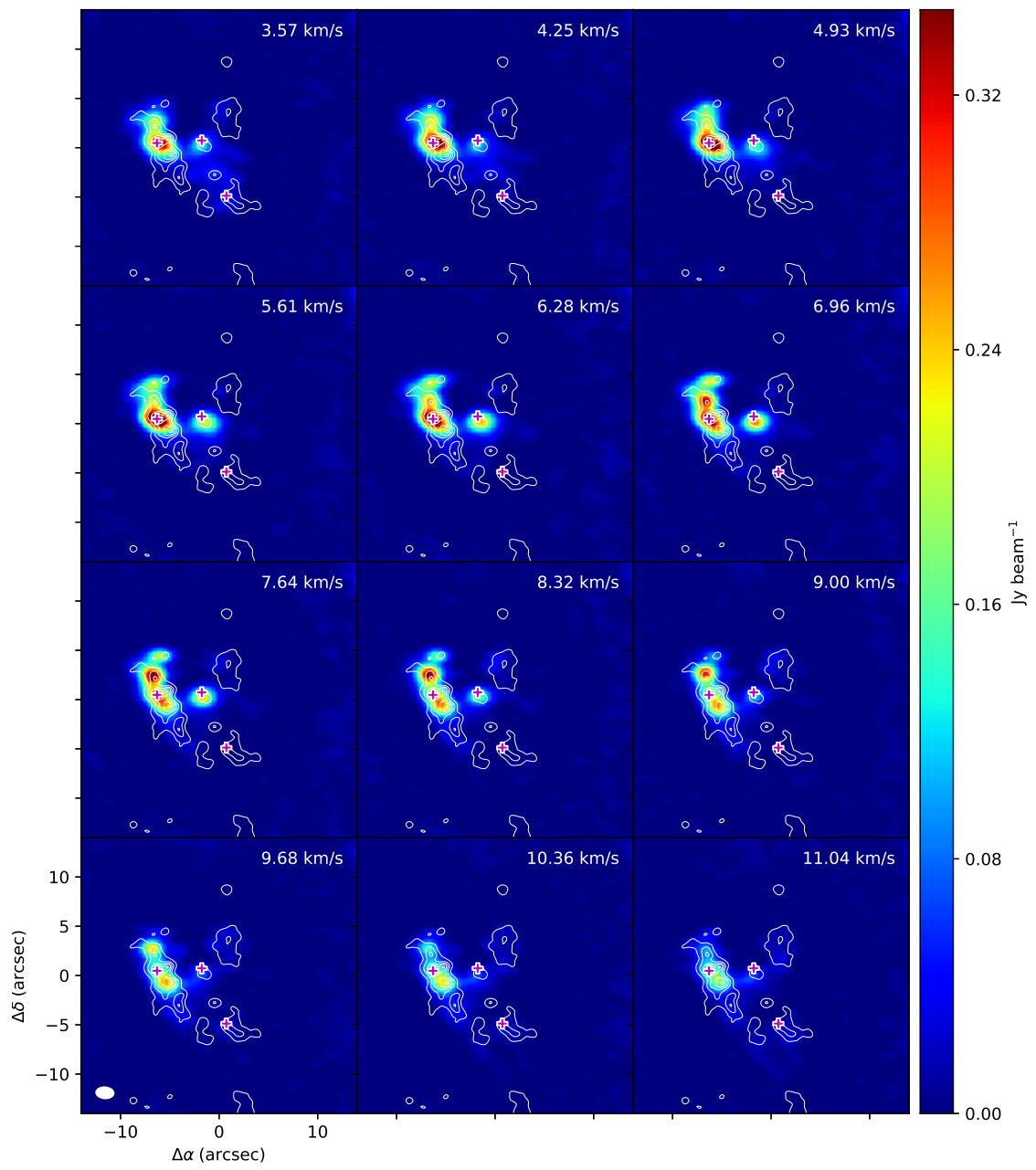


Figure 4.5: Channel map around 215.670 GHz. Same as Figure 3.2 but for white contours and mazenta crosses.

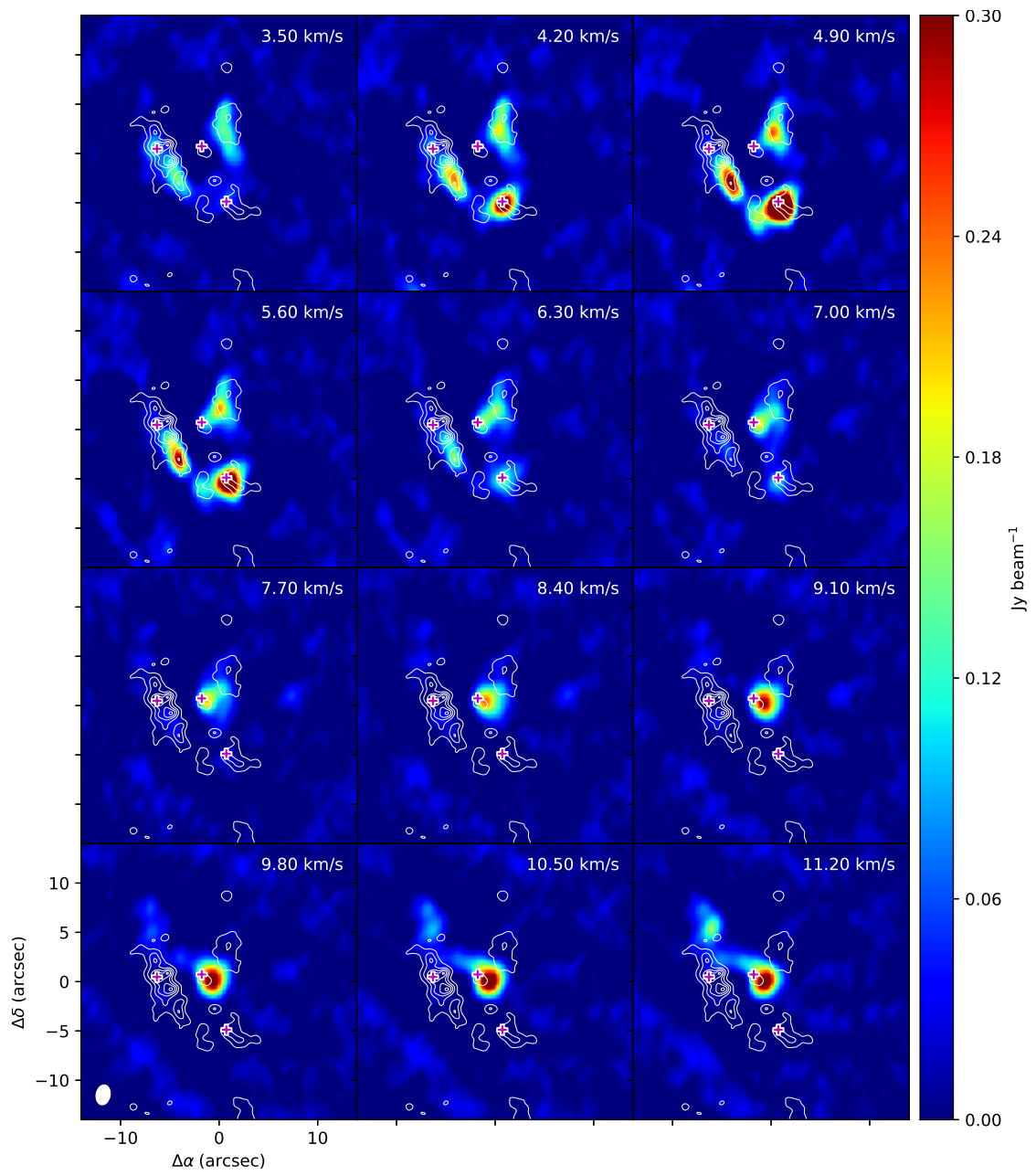


Figure 4.6: Channel map around 221.755 GHz line. Same as Figure 3.2 but for white contours and mazenta crosses.

Chapter 5

Conclusions

In order to ascertain whether the presence of CH_3NH_2 , a precursor of glycine, in the star-formation regions is universal and further to accelerate the discussion regarding the exogenous delivery of prebiotic species to planets and connection between the Universe and life, we explored the existence of CH_3NH_2 in 3 star-forming regions using ALMA archival data.

As a result of the analysis, CH_3NH_2 was not detected in low mass star-forming regions (see Appendix A), but some emission lines were detected in Orion-KL.

According to the analysis, the physical properties of CH_3NH_2 were found as follows.

- From the integrated intensity maps, CH_3NH_2 concentrates in Hot Core.
- V_{LSR} and FWHM line width are estimated to be $4.84 \pm 0.22 \text{ km s}^{-1}$ and $4.16 \pm 0.22 \text{ km s}^{-1}$, respectively. V_{LSR} are consistent with those of N-bearing COMs observed toward Hot core. On the other hand, $\Delta V_{1/2}$ of CH_3NH_2 is narrower than those of other molecule in Hot core.
- By using the rotation diagram method, we evaluated its T_{rot} and N_{MA} to be $95.4^{+15.5}_{-11.7} \text{ K}$, and $(5.5^{+1.6}_{-1.1}) \times 10^{14} \text{ cm}^{-2}$, respectively.

The distribution and spectrum parameters (V_{LSR} and FWHM line width) of CH_3NH_2 in Orion-KL is reported for the first time. Regarding its rotational temperature and column

density, we gave more restrictions than previous studies.

However, since contamination is not sufficiently studied, this detection is still tentative. We need further line identification including other frequency bands to constrain T_{rot} and N_{MA} .

Appendix A

CH₃NH₂ survey in low mass star-forming regions

CH₃NH₂ survey in low mass star-forming regions is also significant, as the low mass star- formation region is considered to be directly related to the origin of the comets. We surveyed not only in Orion-KL but also in the following two low mass star-forming regions, but CH₃NH₂ was not detected. Therefore, we evaluated the upper limit to its column densities as a function of rotational temperature by using the intensity of 3 noise level. We used lines whose $S\mu^2$ value is large in relatively line free regions. We report the results of the analysis briefly.

A.1 IRAS 16293

IRAS 16293 is a binary system of two stars, of which source B has narrower line width ($\sim 1.0 \text{ km s}^{-1}$) and is suitable for line survey (Persson et al., 2018). The CH₃NH₂ survey in this region has been done (Ligterink et al., 2018), but CH₃NH₂ was not detected. In this paper, they used ALMA band 7 data and analyzed the spectrum extracted from an offset position toward source B. Therefore, we performed additional analysis in other band without applying spatial bias. The line survey procedure is the same up to no.2 in

Section 2.2.2.

A.1.1 Observation data

ALMA Band 6 archive data of PILS survey was used (#2012.1.00712.S, Jørgensen et al. (2016)). These data cube were already calibrated by Oya et al. (2016). The backend correlator was tuned to a resolution of 122 kHz, which corresponds to a velocity resolution of 0.15 km s^{-1} at 240 GHz. Details of each data are summarized in Table A.1.

Table A.1: Summary of Observations for IRAS 16293

	Window	Frequency range [GHz]	Date	FWHM	PA
B6-1	0	239.40-239.86	2014-Jun.-14	0.48'' \times 0.43''	15
	1	240.15-240.51			
	2	224.75-225.21			
	3	221.76-222.22			
B6-2	0	247.32-247.79	2014-May.-22	0.62'' \times 0.48''	77
	1	250.28-250.75			
	2	231.03-231.51			
	3	232.18-232.65			

A.1.2 Results

There were 4 CH_3NH_2 emission lines that were predicted not to be contaminated by other molecular emission lines within the observation frequency coverage, but in any case, radiation exceeding 3σ noise level were not be confirmed. Figure A.1 is an example of integrated intensity map. Since FWHM line width of IRAS 16293 B is $\Delta V_{1/2} \sim 1.0 \text{ km s}^{-1}$ and $1\sigma = 3.8 \text{ mJy}$, signals less than $11.4 \text{ mJy beam}^{-1} \text{ km s}^{-1}$ are not regarded as significant.

The column density can be obtained by transforming Equation 4.1 as follows.

$$N_{\text{MA}} = U_{\text{rot}} \times \frac{3 k_{\text{B}} T_{\text{B}} \Delta V_{1/2}}{8 \pi^3 \nu S \mu_0^2} \times 10^{E_{\text{u}}/k_{\text{B}} T_{\text{rot}}} \times e \quad (\text{A.1})$$

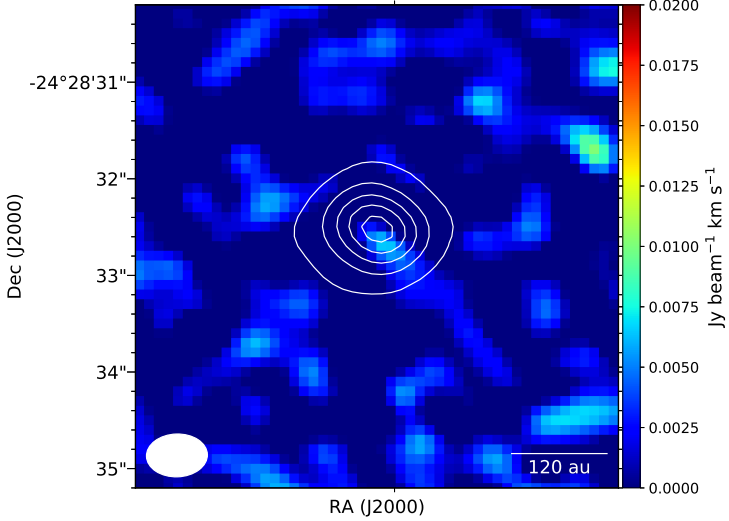


Figure A.1: Integrated intensity map around 247.362 GHz. The white contours represent the 1.3 mm continuum map, where the contour levels are 10 %, 30 %, 50 %, 70 %, 90 % of the peak intensity of 0.65 Jy/beam.

The upper limit column densities of CH_3NH_2 have been determined for rotational temperatures between 70 and 130 K. These are plotted in Figure A.2. The upper limit column densities of CH_3NH_2 are determined on the $7_2E_{1-1} \rightarrow 7_1E_{1-1}$ transition at 247.362 GHz ($S\mu^2 = 33.68 \text{ D}^2$) for a 3σ line intensity of $3.8 \text{ mJy beam}^{-1}$.

The order of the obtained value of CH_3NH_2 was about 13. Compared to the column density of detected N-bearing COMs (e.g., $4.4_{-1.9}^{+3.0} \times 10^{14} \text{ cm}^{-2}$ for NH_2CHO , Kahane et al., 2013), the upper limit of CH_3NH_2 seems to be consistent.

A.2 L483

CH_3NH_2 survey in L483 has not been reported so far. Therefore we attempted exploration of CH_3NH_2 for the first time using ALMA Band 6 archive data (#2016.1.01325.S. PI: Yoko Oya).

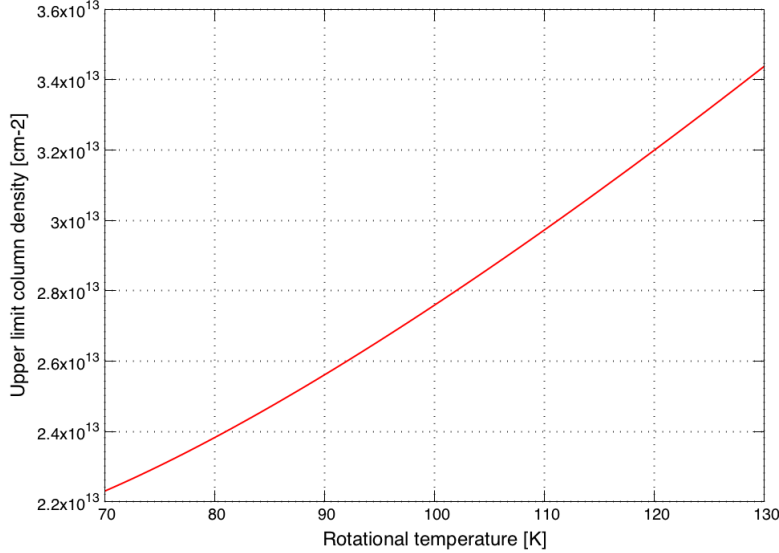


Figure A.2: Upper limit column density for the strongest CH_3NH_2 transition ($7_2E_{1-1} \rightarrow 7_1E_{1-1}$) as function of T_{rot} . A 3σ value of $11.4 \text{ mJy beam}^{-1}$ is used.

A.2.1 Observation data

ALMA data cube were already calibrated and reduced by Oya et al. Details of each data are summarized in Table A.2

A.2.2 Results

There were 12 CH_3NH_2 emission lines that were predicted not to be contaminated by other molecular emission lines within the observation frequency coverage, but in any case, radiation exceeding 3σ noise level were not be confirmed. Figure A.3 is an example of integrated intensity map. The rms noise level of this data was 7.5 mJy . Assuming FWHM line width of L483 is $\Delta V_{1/2} \sim 6.0 \text{ km s}^{-1}$ (Oya et al., 2017), signals less than $135 \text{ mJy beam}^{-1} \text{ km s}^{-1}$ are not regarded as significant.

Similar to IRAS 16293 B, the upper limit column densities of CH_3NH_2 have been determined for rotational temperatures between 70 and 130 K. The upper limit column densities of CH_3NH_2 are determined on the $11_2A_1 \rightarrow 11_1A_2$ transition at 217.079 GHz ($S\mu^2 = 39.11 \text{ D}^2$) for a 3σ line intensity of $22.5 \text{ mJy beam}^{-1}$. These are plotted in

Table A.2: Summary of Observations for L483

Window	Frequency range [GHz]	Channel width [KHz]
0	217.054675-217.113267	122.07
1	218.188881-218.247473	122.07
2	218.4246824-218.483274	122.07
3	218.7137034-218.772295	122.07
4	219.5166704-219.575262	122.07
5	219.7756644-219.834256	122.07
6	219.9161004-219.974692	122.07
7	220.7136484-220.772240	122.07
8	236.479210-236.5378016	122.07
9	235.124431-235.1830226	122.07
10	235.944439-236.0030306	122.07
11	236.701431-236.7600226	122.07
12	232.748687-232.9830534	488.28
13	232.466563-232.7009295	488.28
14	244.5532143-244.611806	122.07
15	243.8820343-243.940626	122.07
16	244.2362093-244.294801	122.07
17	244.9017733-244.960365	122.07
18	247.1782195-247.412586	488.28
19	245.5792095-245.813576	488.28
20	262.359554-262.4181457	122.07
21	262.181917-262.2405087	122.07
22	263.708901-263.8260843	122.07
23	261.795953-261.8545447	122.07
24	260.496957-260.5555487	122.07
25	262.057967-262.1165587	122.07
26	261.282971-261.3415627	122.07

Figure A.4.

The order of the obtained value of CH_3NH_2 was about 15. Compared to the column density of detected N-bearing COMs (e.g., $1.2 \sim 1.9 \times 10^{14} \text{ cm}^{-2}$ for NH_2CHO , Oya et al., 2017), the upper limit of CH_3NH_2 seems to be overestimated. This overestimation seems to be derived from inappropriate line width selection. According to Oya et al. (2017), it has been found that molecules trace different region, so that the line width is different. $\Delta V_{1/2} \sim 6.0 \text{ km s}^{-1}$ was derived from the simple molecules. Since the line width of N-bearing species is narrow, it is estimated that the actual upper limit would be smaller.

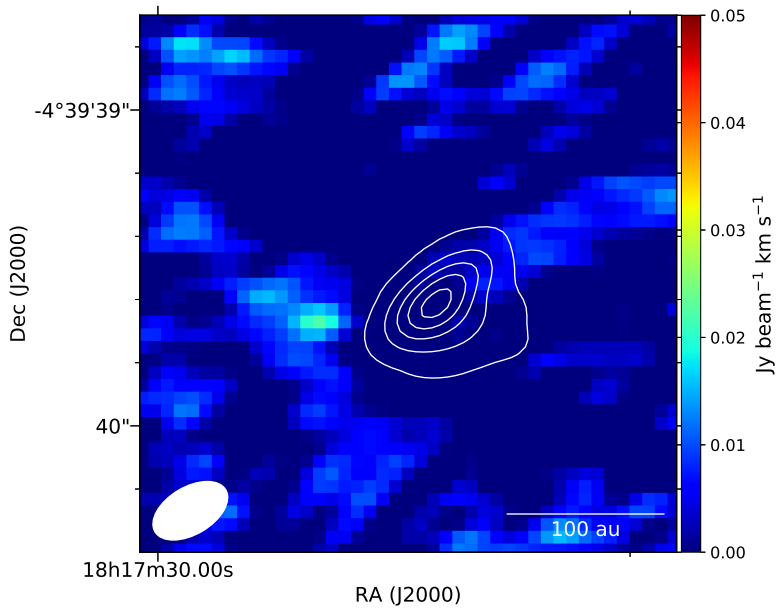


Figure A.3: Integrated intensity map around 217.079 GHz. The white contours represent the 1.3 mm continuum map, where the contour levels are 10 %, 30 %, 50 %, 70 %, 90 % of the peak intensity of 11 mJy/beam.

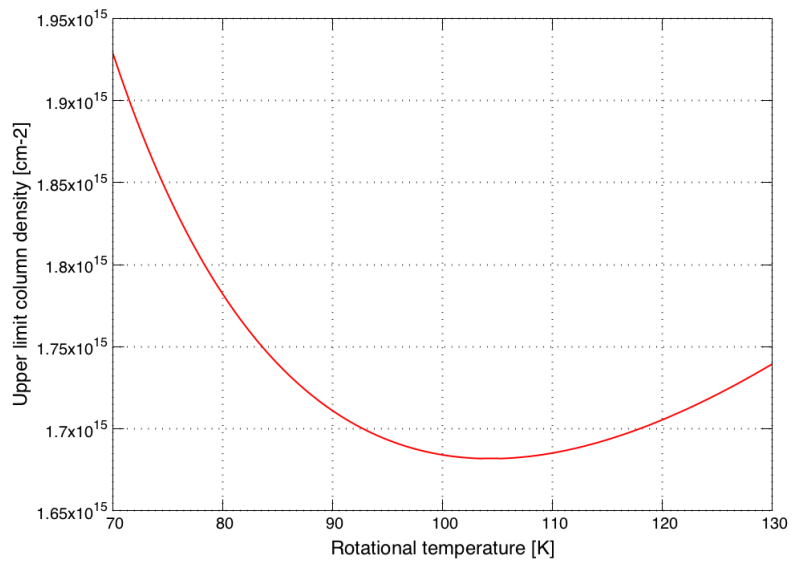


Figure A.4: Upper limit column density for the strongest CH_3NH_2 transition ($11_2A_1 \rightarrow 11_2A_2$) as function of T_{rot} . A 3σ value of $22.5 \text{ mJy beam}^{-1}$ is used.

Appendix B

Distribution of CH₃NH₂ lines contaminated by other molecular line emission in Orion-KL

B.1 Integrated intensity maps

Out of 24 selected transitions in our observational frequency range, 16 CH₃NH₂ transitions are blended or masked by other spectral features, or its signal are below the noise level.

In Appendix B, we list 16 transitions that we could not detect.

Table B.1: Summary of transition

Frequency [GHz]	$S\mu^2$ [D ²]	E _u [K]	Transition (J, K_a, Γ)	Noise [K]	Comments
222.846	117.24	156.55	11, 2, $B_1 \rightarrow 11, 1, B_2$	0.084	SV data
227.545	105.11	133.16	10, 2, $B_2 \rightarrow 10, 1, B_1$	0.351	SV data
231.844	93.40	111.90	9, 2, $B_1 \rightarrow 9, 1, B_2$	0.462	SV data
242.625	56.31	399.37	18, 3, $B_2 \rightarrow 17, 4, B_1$	0.534	SV data
231.524	55.71	399.38	18, 3, $E_{1-1} \rightarrow 17, 4, E_{1-1}$	0.035	Reported in Pagani+17
218.221	50.47	59.97	7, 0, $E_{1+1} \rightarrow 6, 1, E_{1+1}$	3.639	
219.151	42.23	92.22	8, 2, $E_{1-1} \rightarrow 8, 1, E_{1+1}$	0.065	
227.997	39.83	92.64	8, 2, $E_{1+1} \rightarrow 8, 1, E_{1+1}$	0.118	SV data
231.061	38.44	75.61	7, 2, $E_{1+1} \rightarrow 7, 1, E_{1+1}$	1.057	
233.802	35.87	60.71	6, 2, $E_{1+1} \rightarrow 6, 1, E_{1+1}$	0.024	
231.576	35.30	239.73	14, 2, $E_{1+1} \rightarrow 13, 3, E_{1+1}$	0.033	Reported in Pagani+17
216.843	34.42	132.81	10, 2, $E_{2+1} \rightarrow 10, 1, E_{2+1}$	0.074	
251.128	33.32	92.22	8, 2, $E_{1-1} \rightarrow 8, 1, E_{1-1}$	0.153	
218.409	32.65	17.30	3, 1, $E_{1+1} \rightarrow 2, 0, E_{1+1}$	0.059	
217.6701	32.53	156.54	11, 2, $E_{1+1} \rightarrow 11, 1, E_{1+1}$	0.033	Reported in Pagani+17
237.143	14.76	21.99	2, 2, $E_{1-1} \rightarrow 2, 1, E_{1-1}$	0.048	Reported in Pagani+17

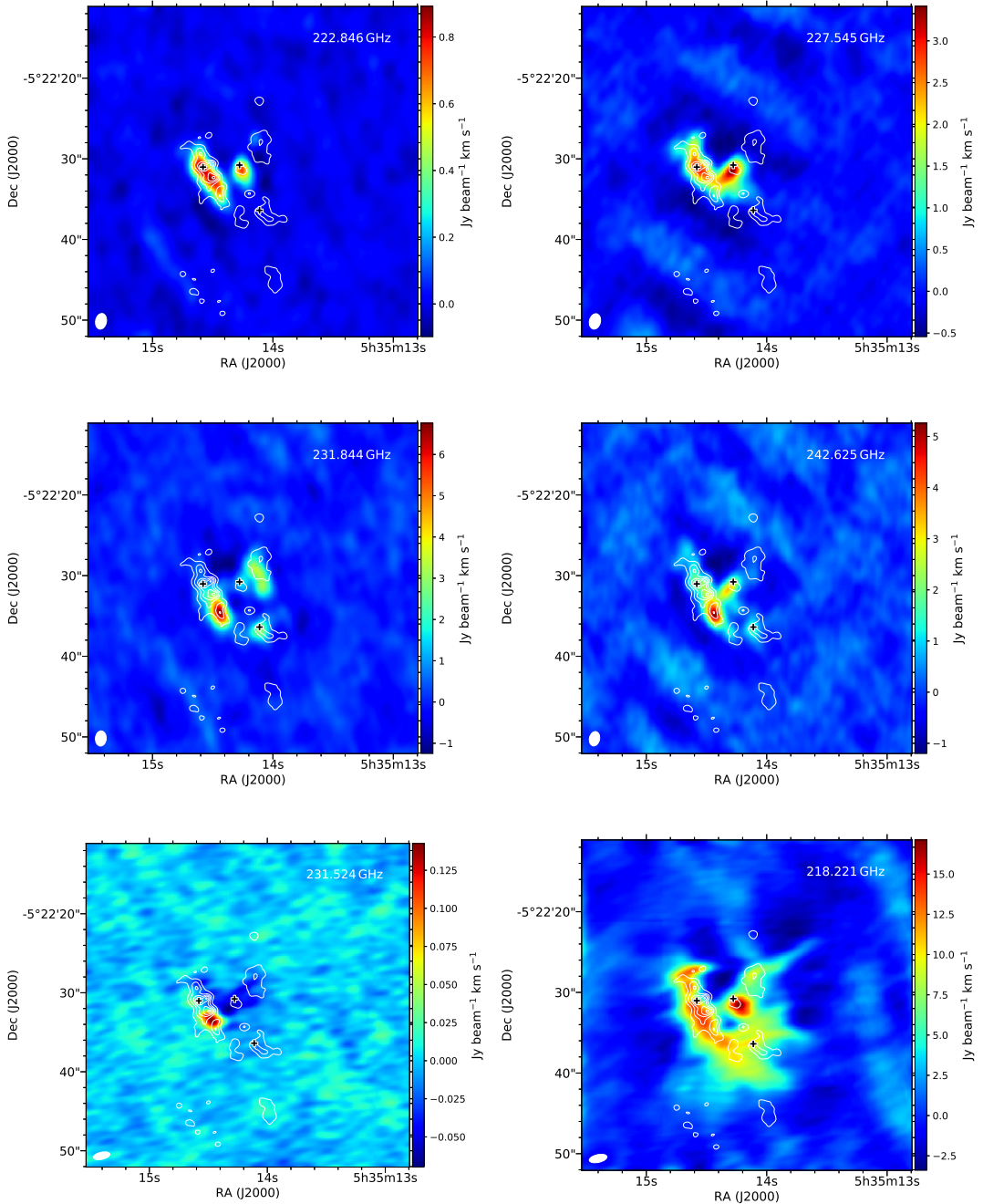


Figure B.1: Integrated intensity maps around CH_3NH_2 line.

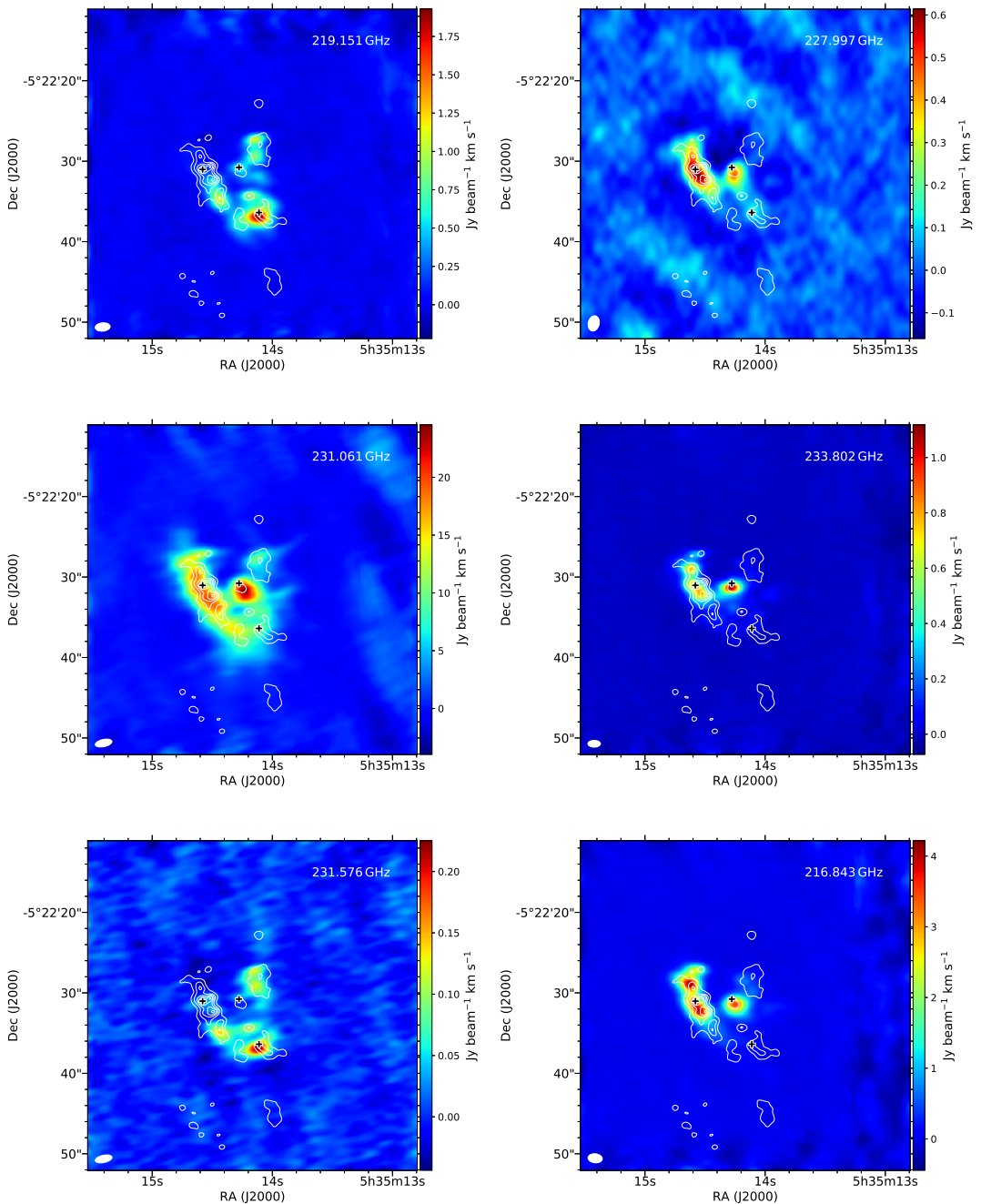


Figure B.2: (Continued)

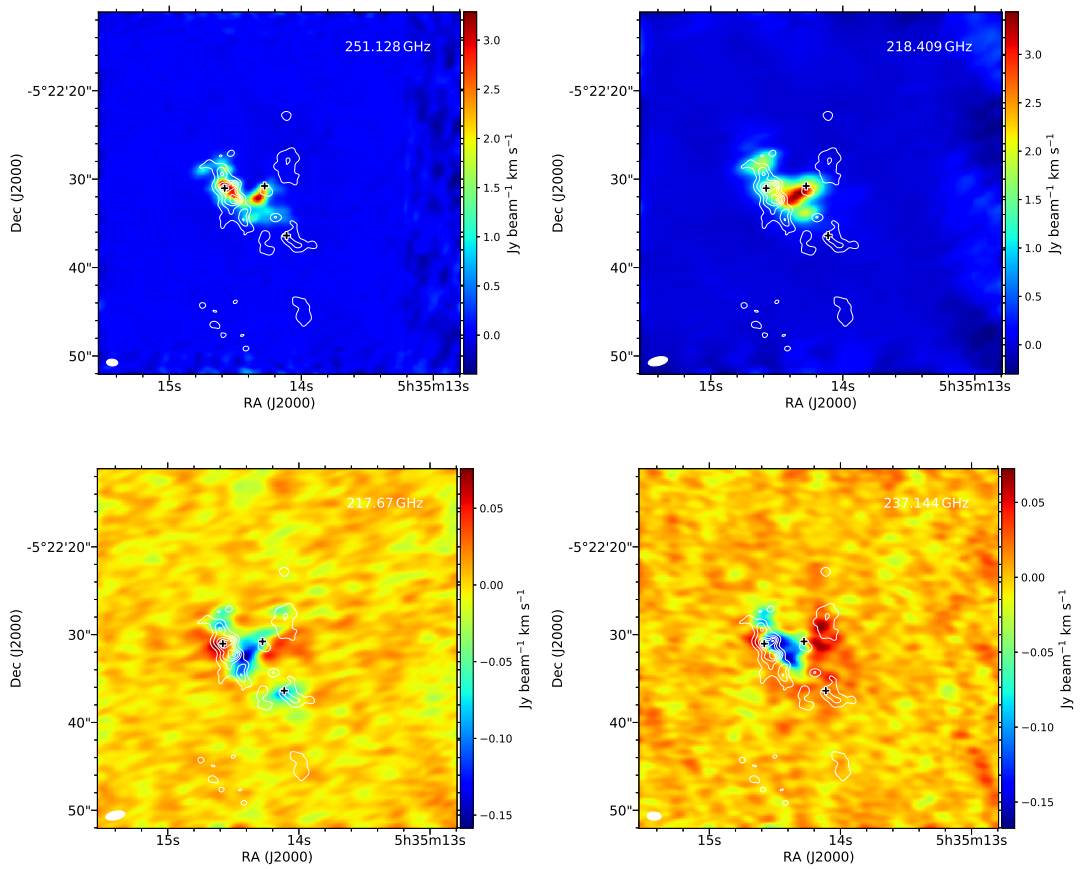


Figure B.3: (Continued)

B.2 Channel maps

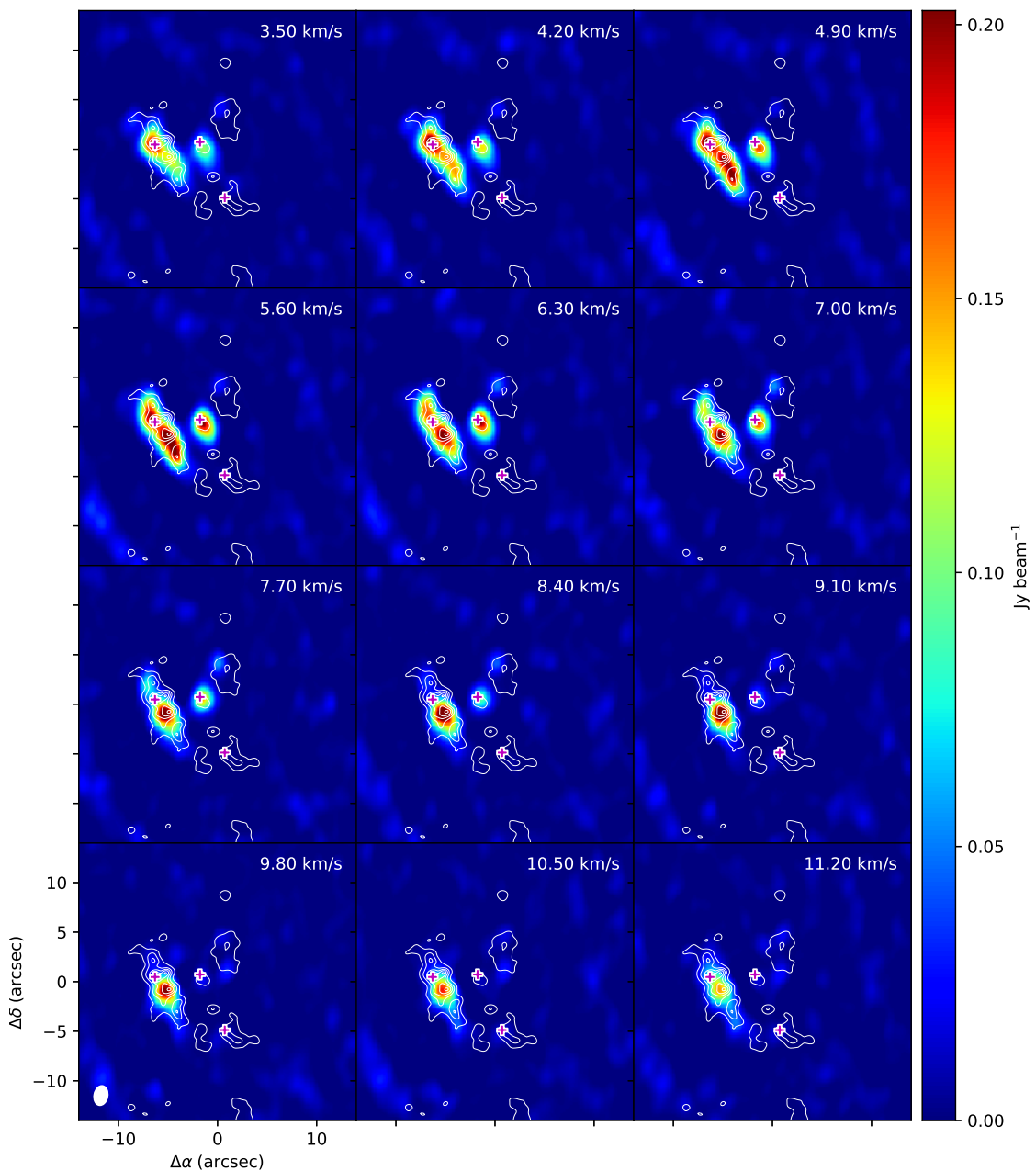


Figure B.4: 222.846 GHz

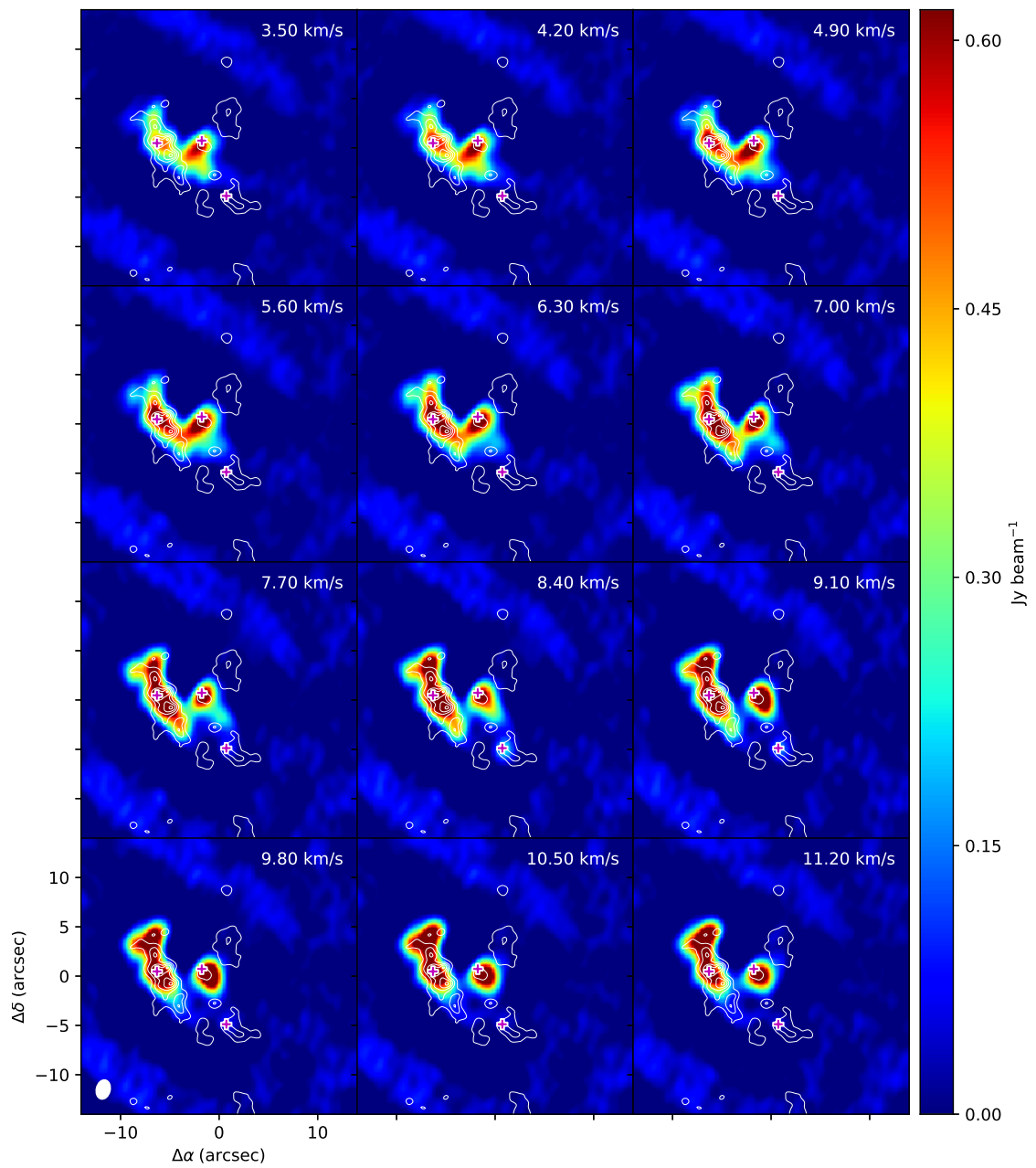


Figure B.5: 227.545 GHz

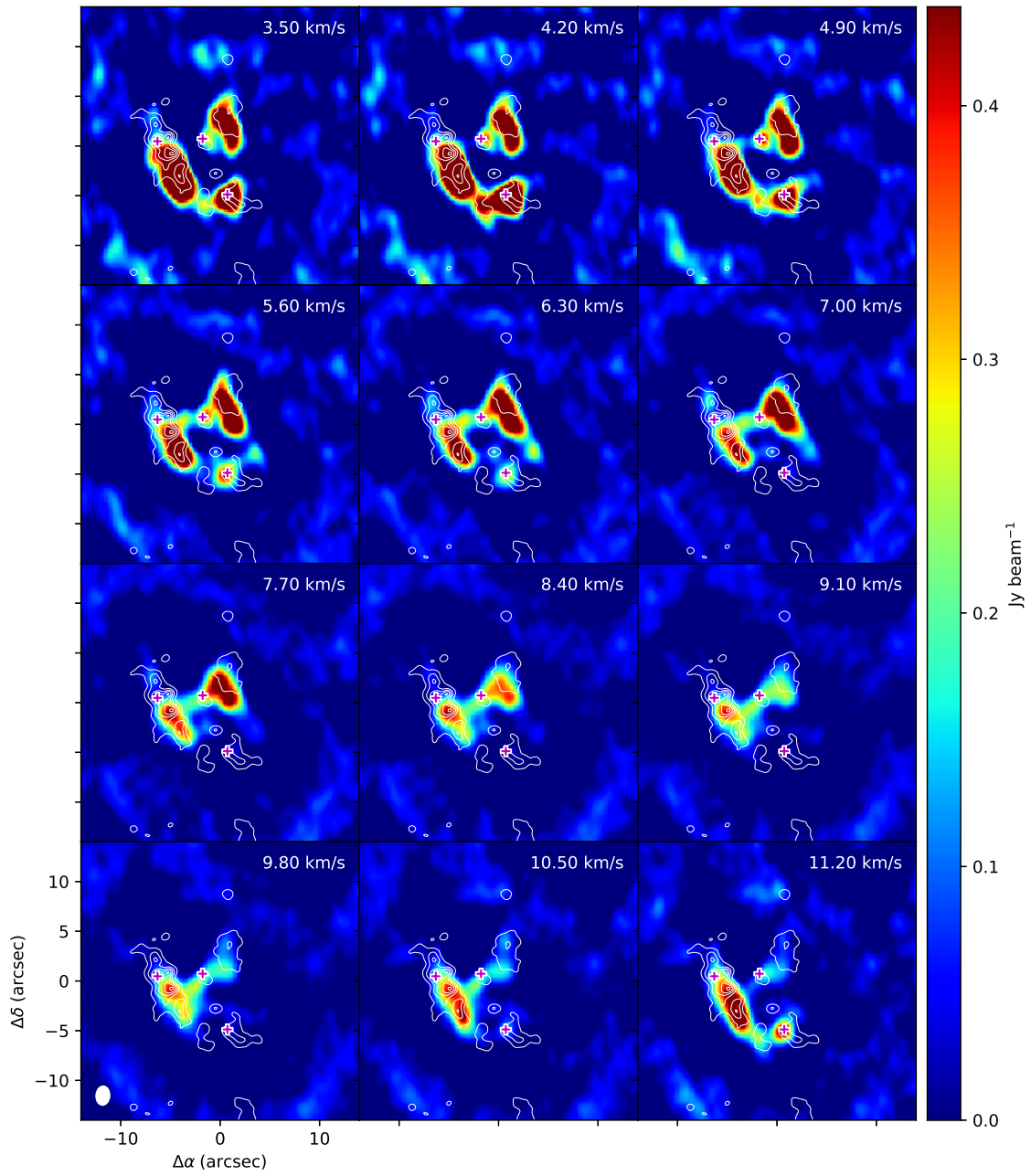


Figure B.6: 231.844 GHz

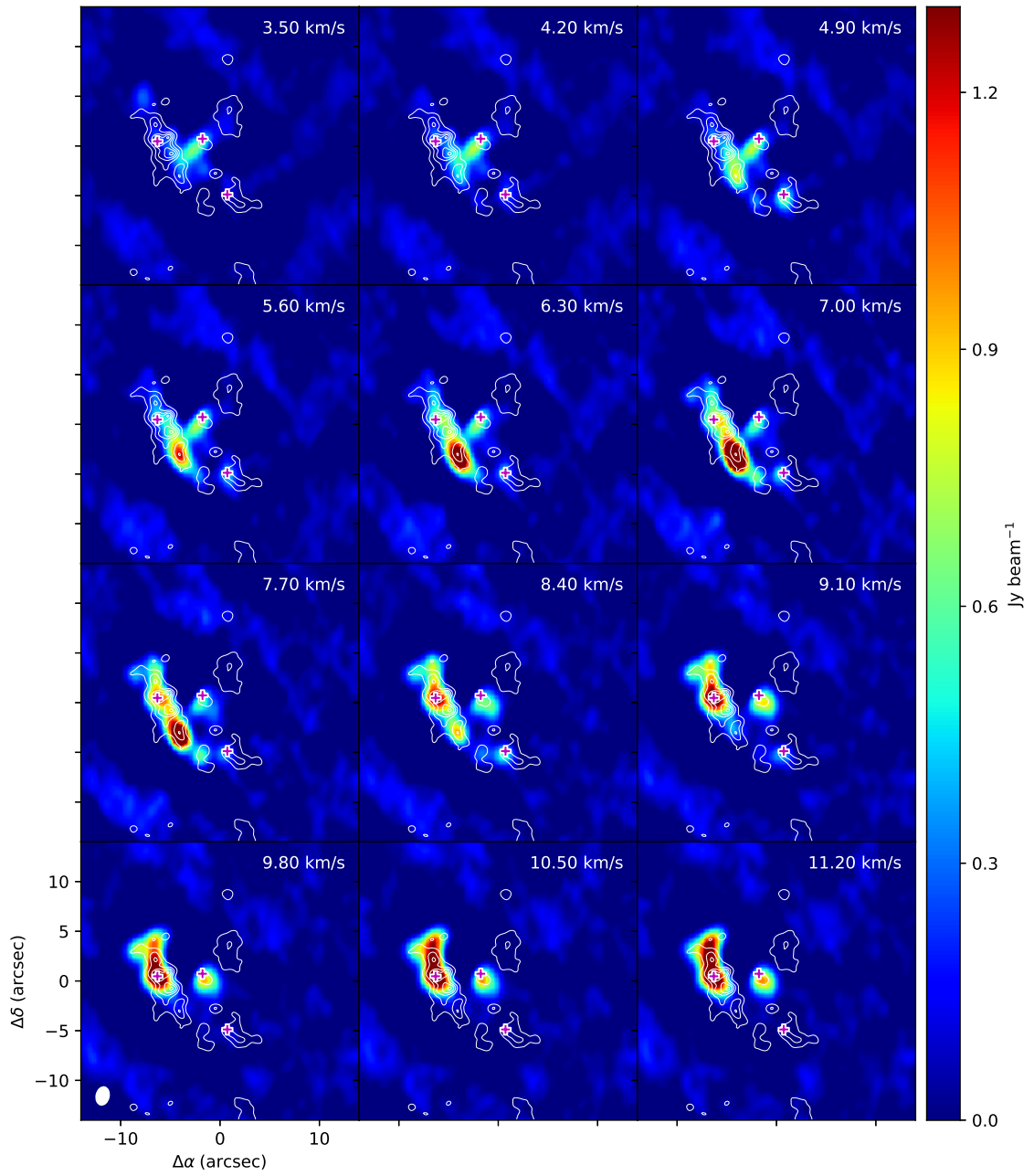


Figure B.7: 242.625 GHz

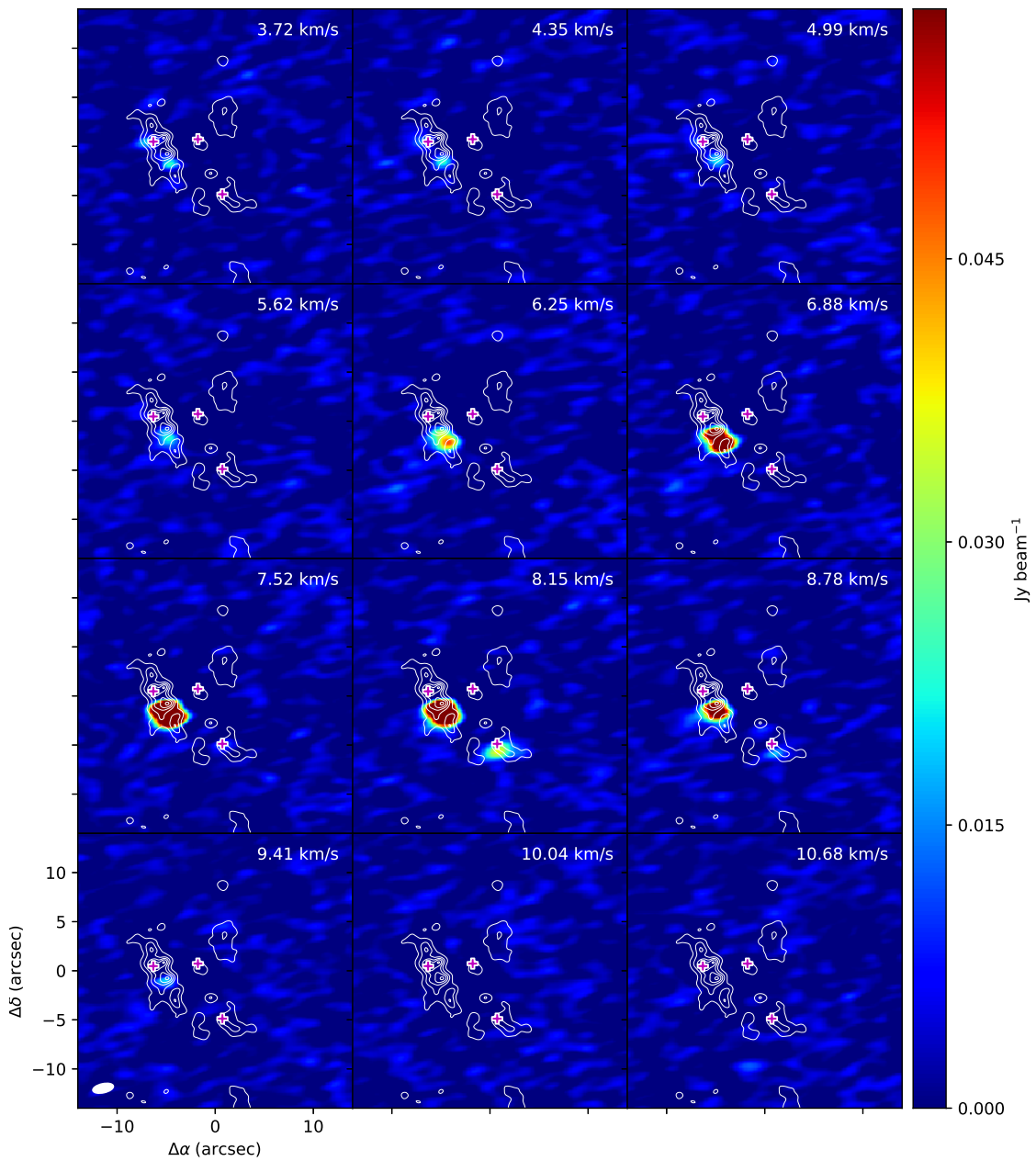


Figure B.8: 231.524 GHz

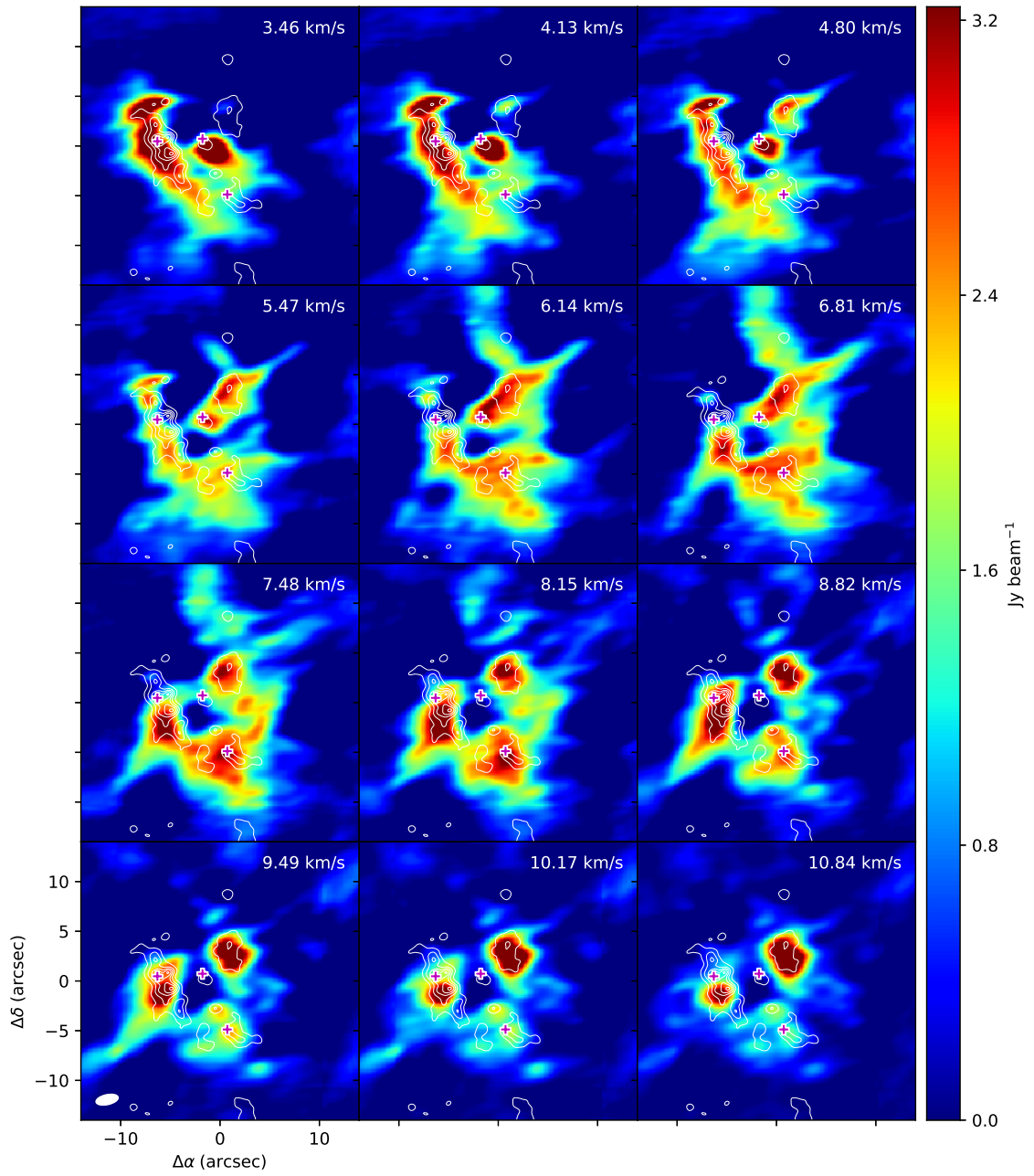


Figure B.9: 218.221 GHz

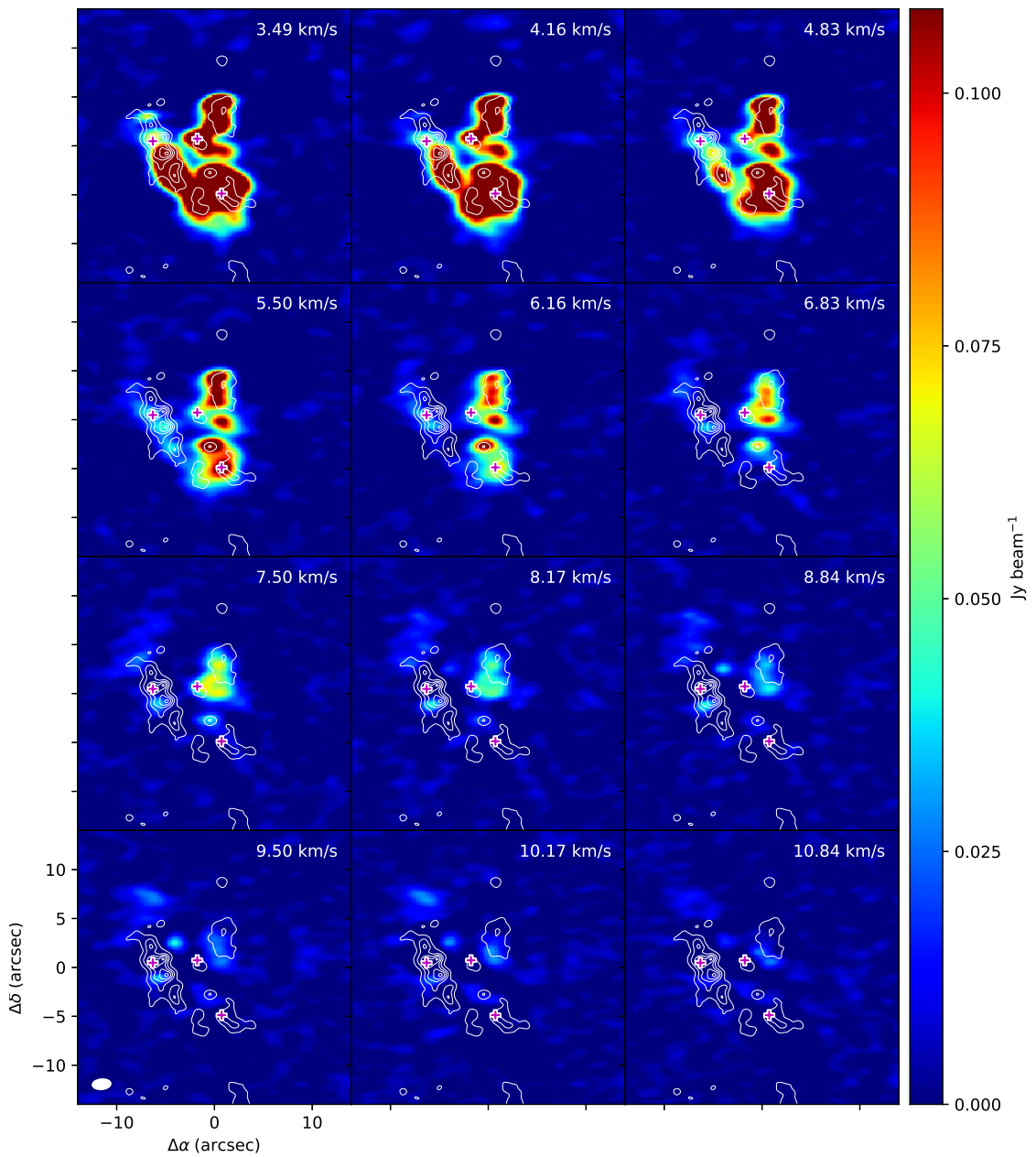


Figure B.10: 219.151 GHz

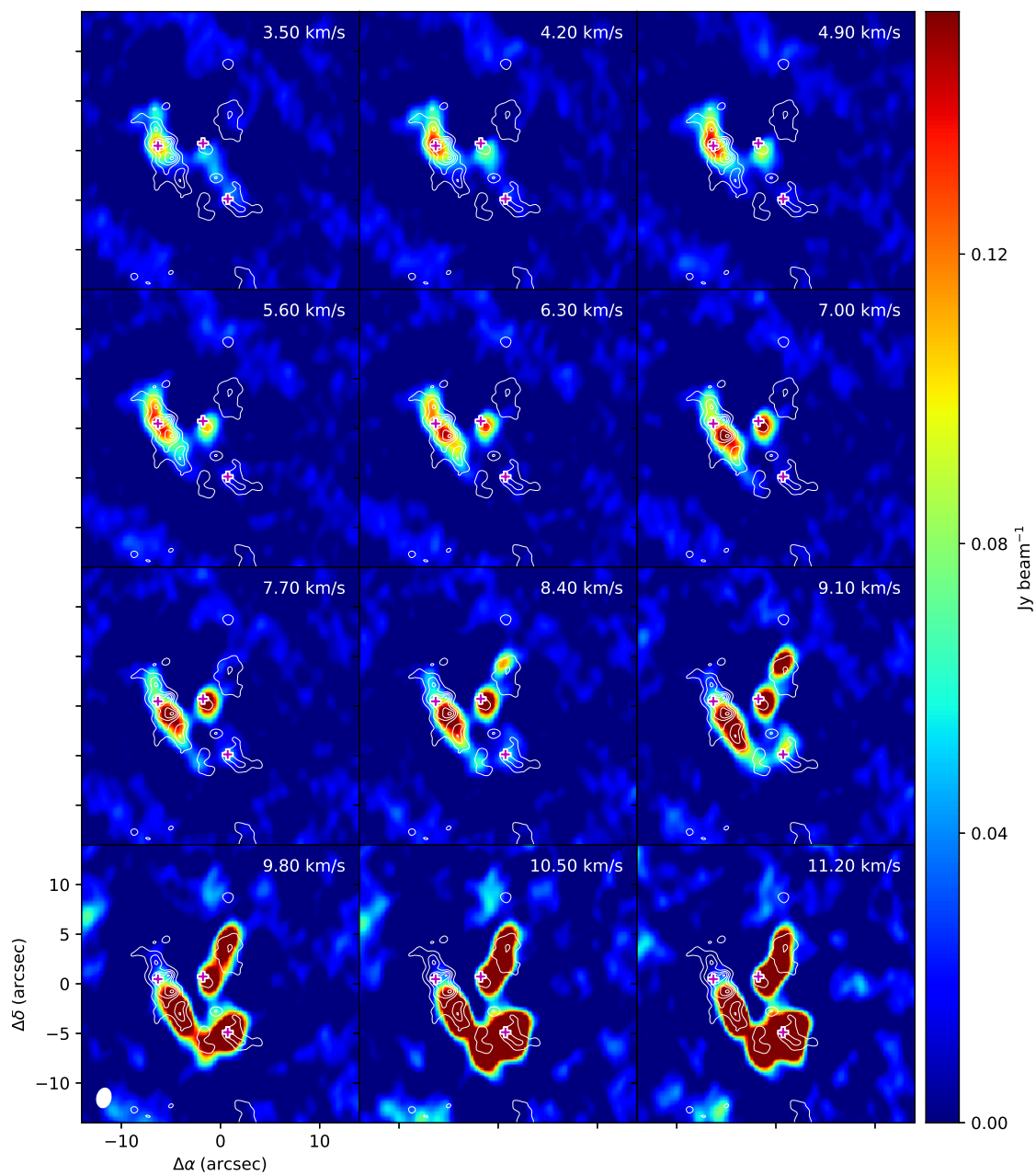


Figure B.11: 227.997 GHz

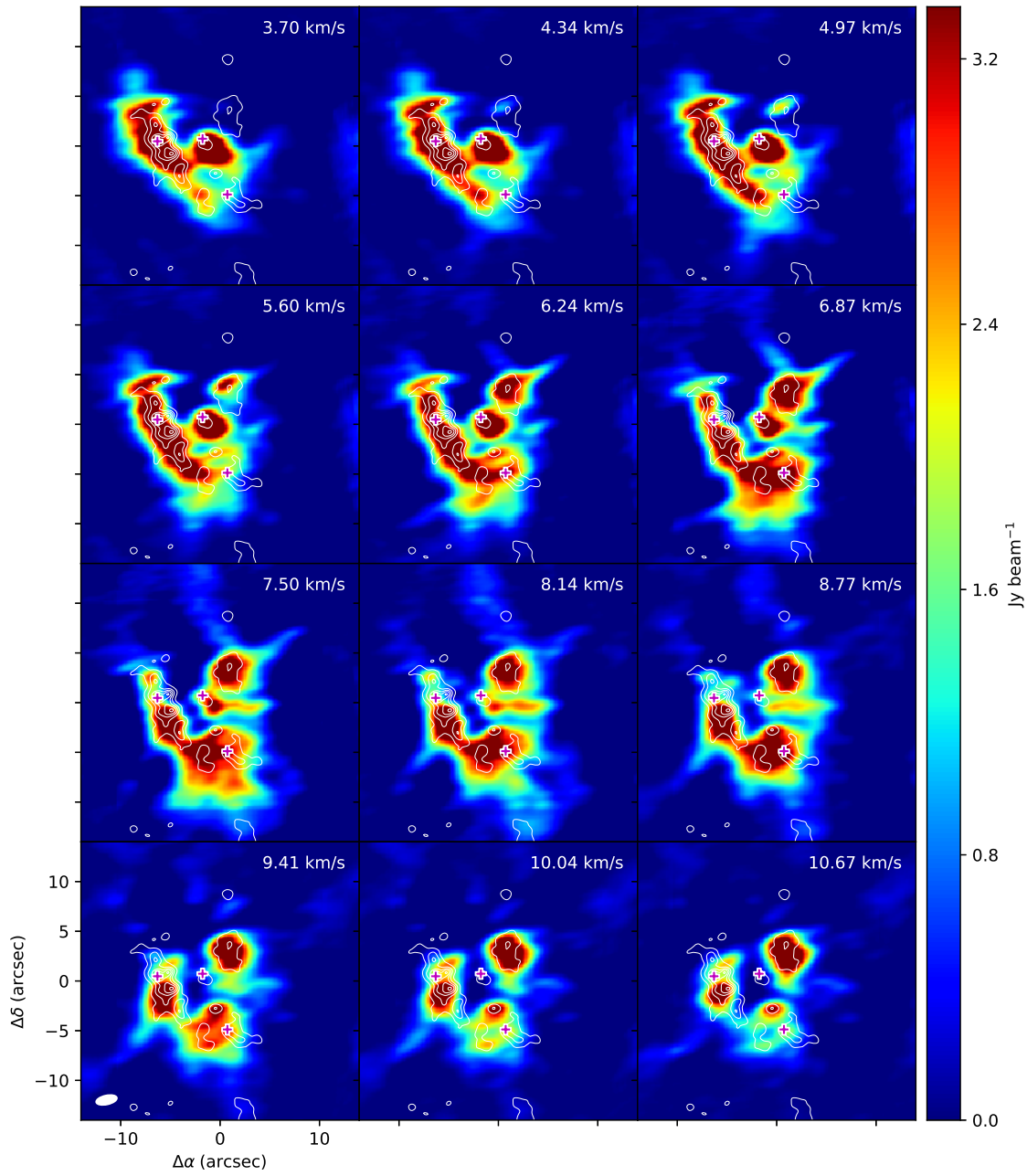


Figure B.12: 231.061 GHz

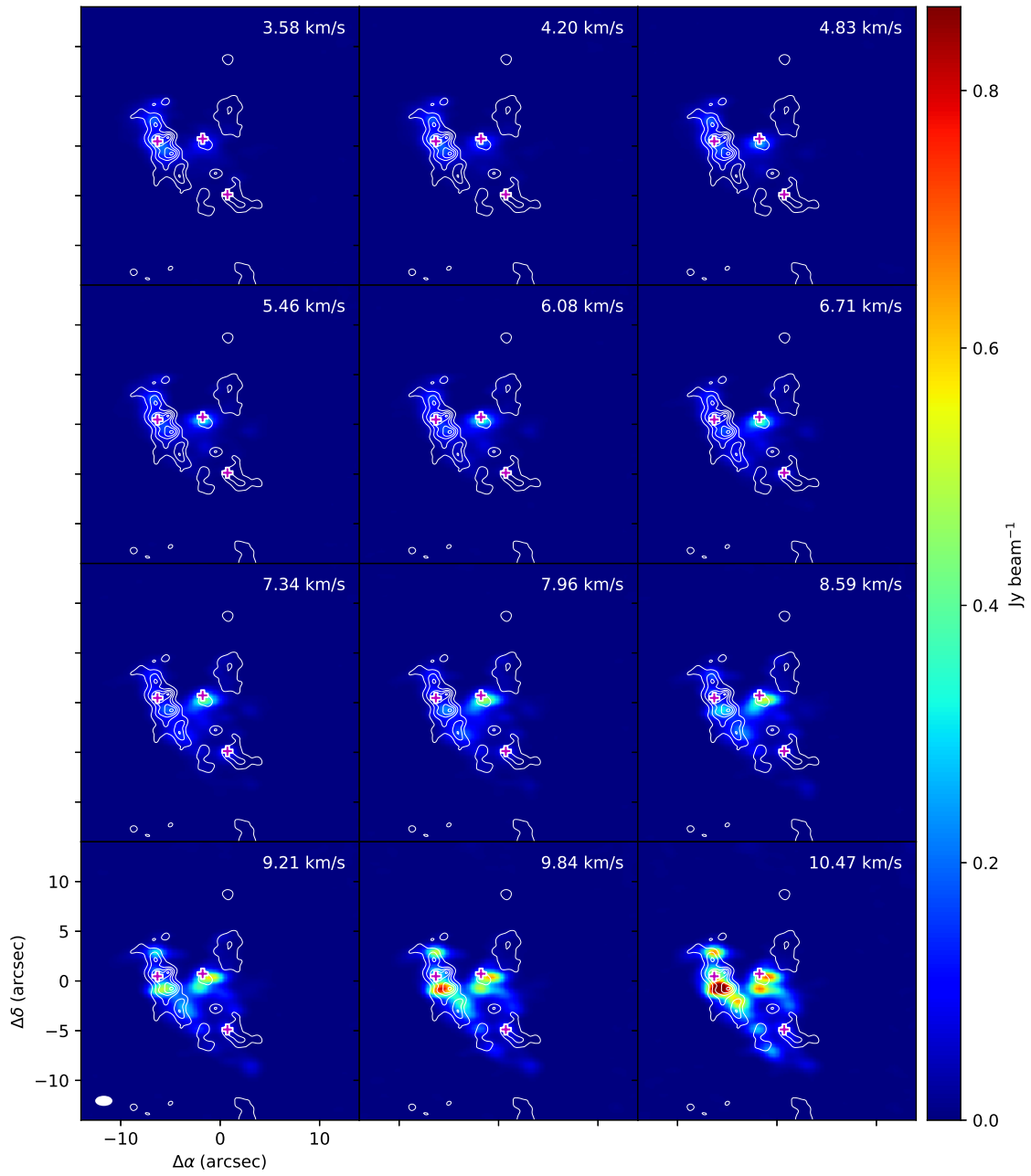


Figure B.13: 233.802 GHz

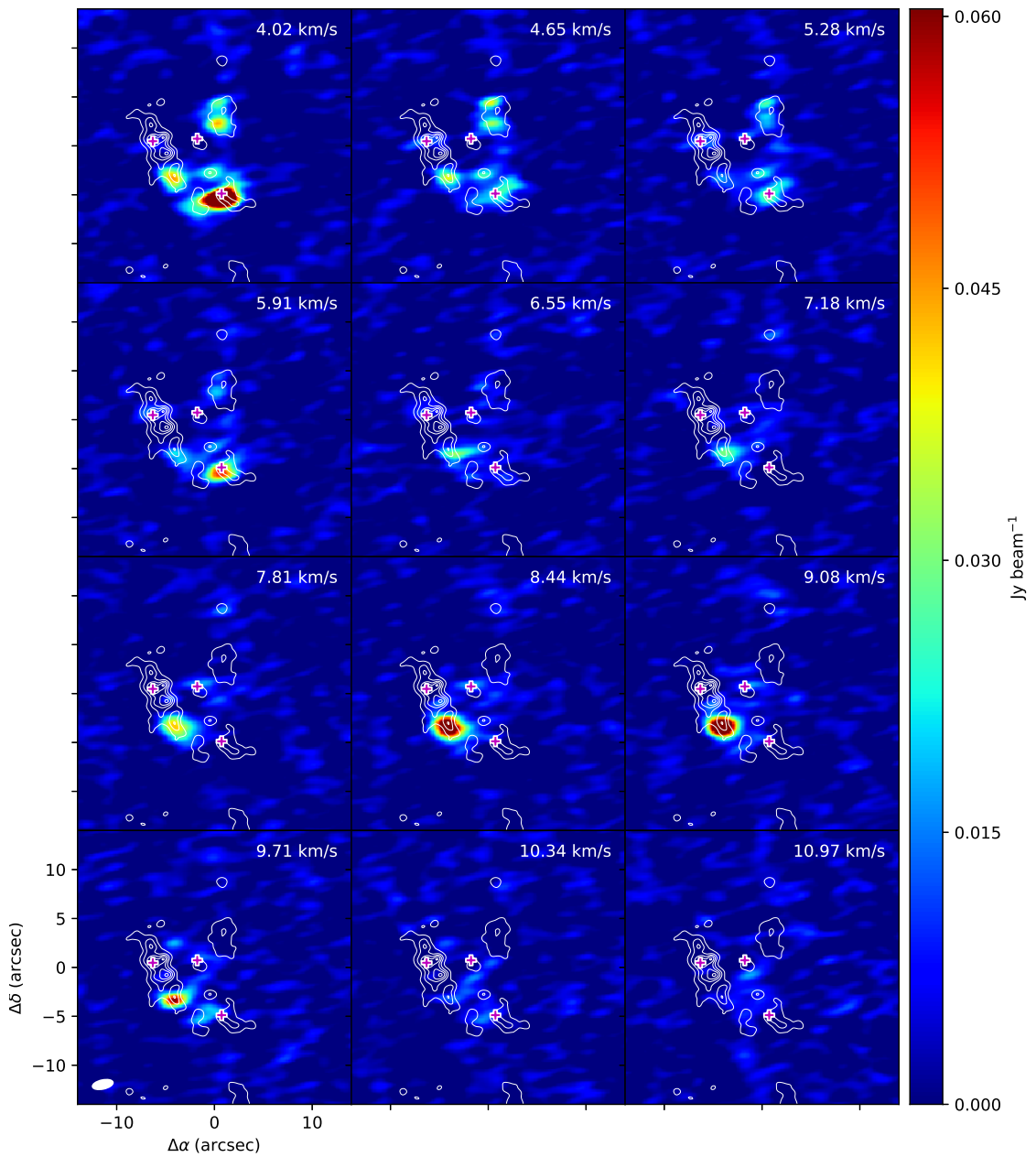


Figure B.14: 231.576 GHz

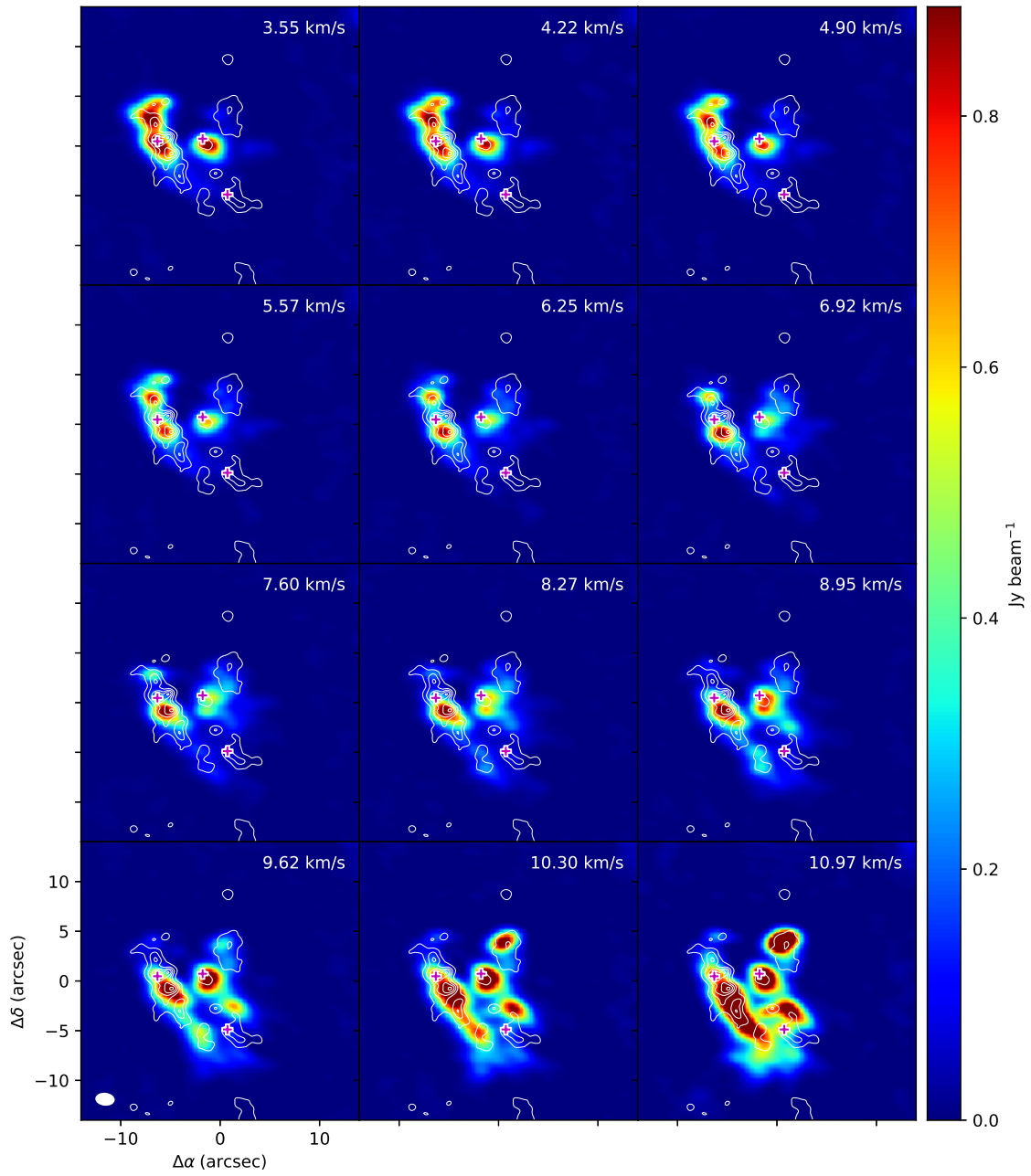


Figure B.15: 216.843 GHz

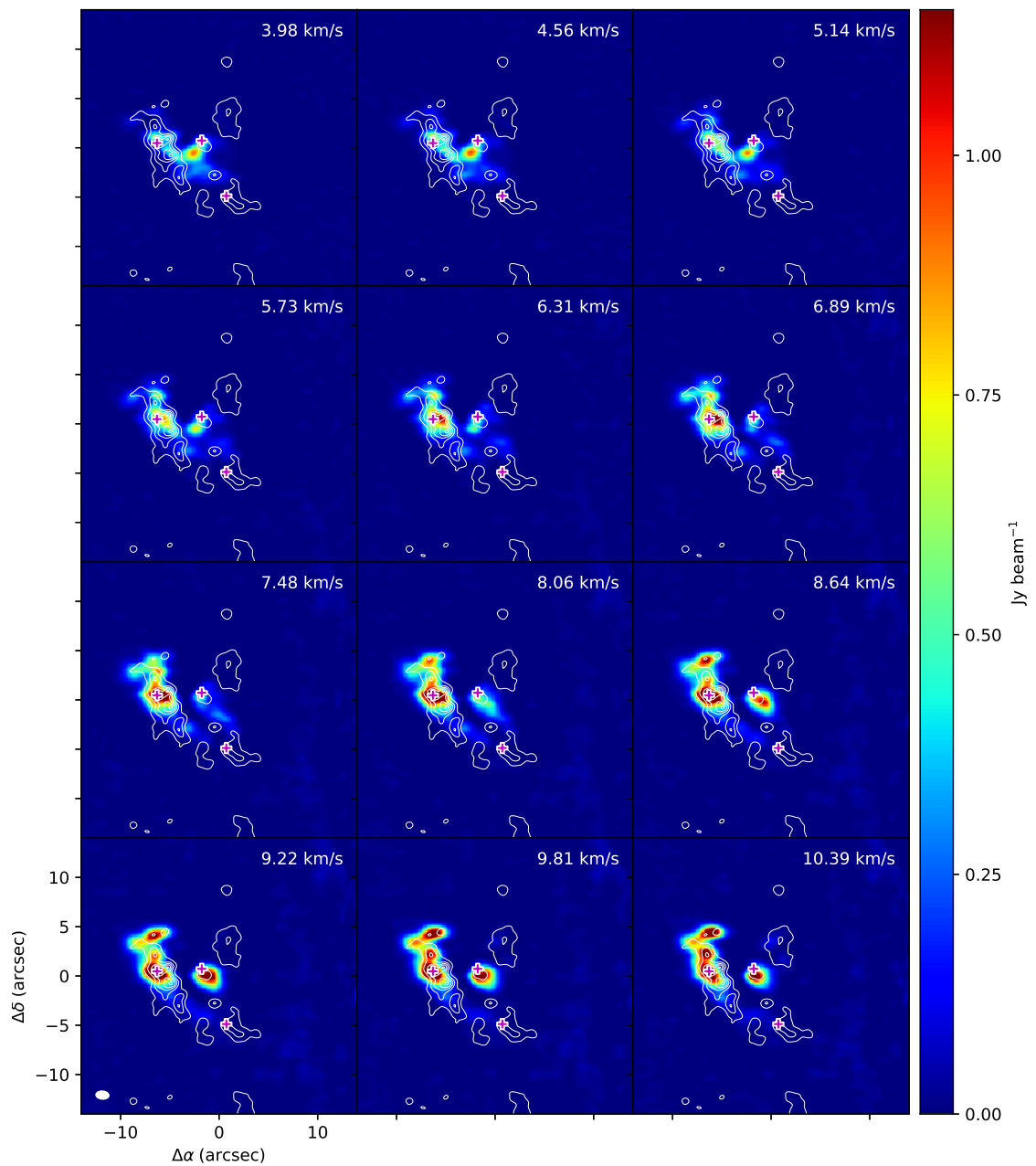


Figure B.16: 251.128 GHz

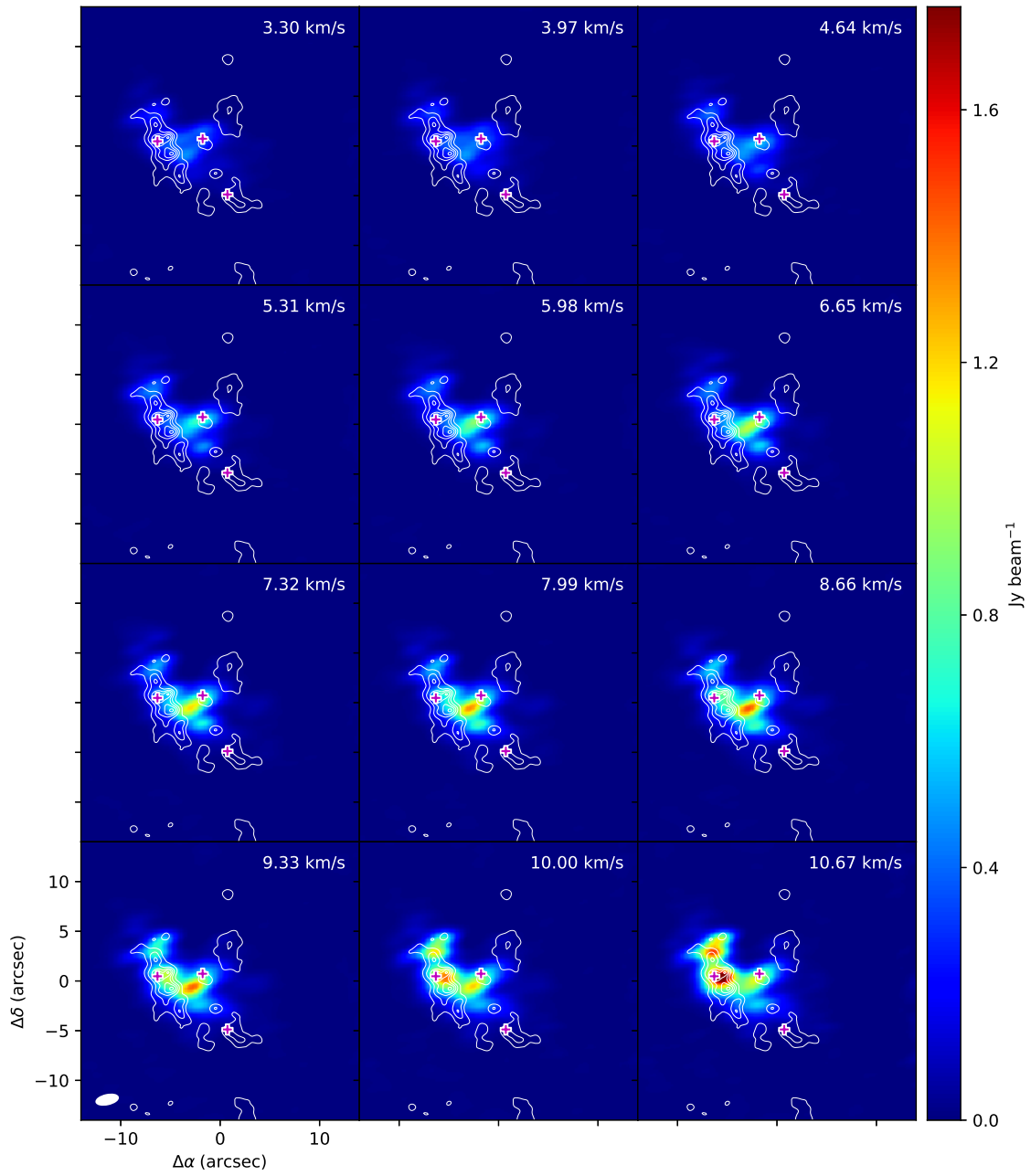


Figure B.17: 218.409 GHz

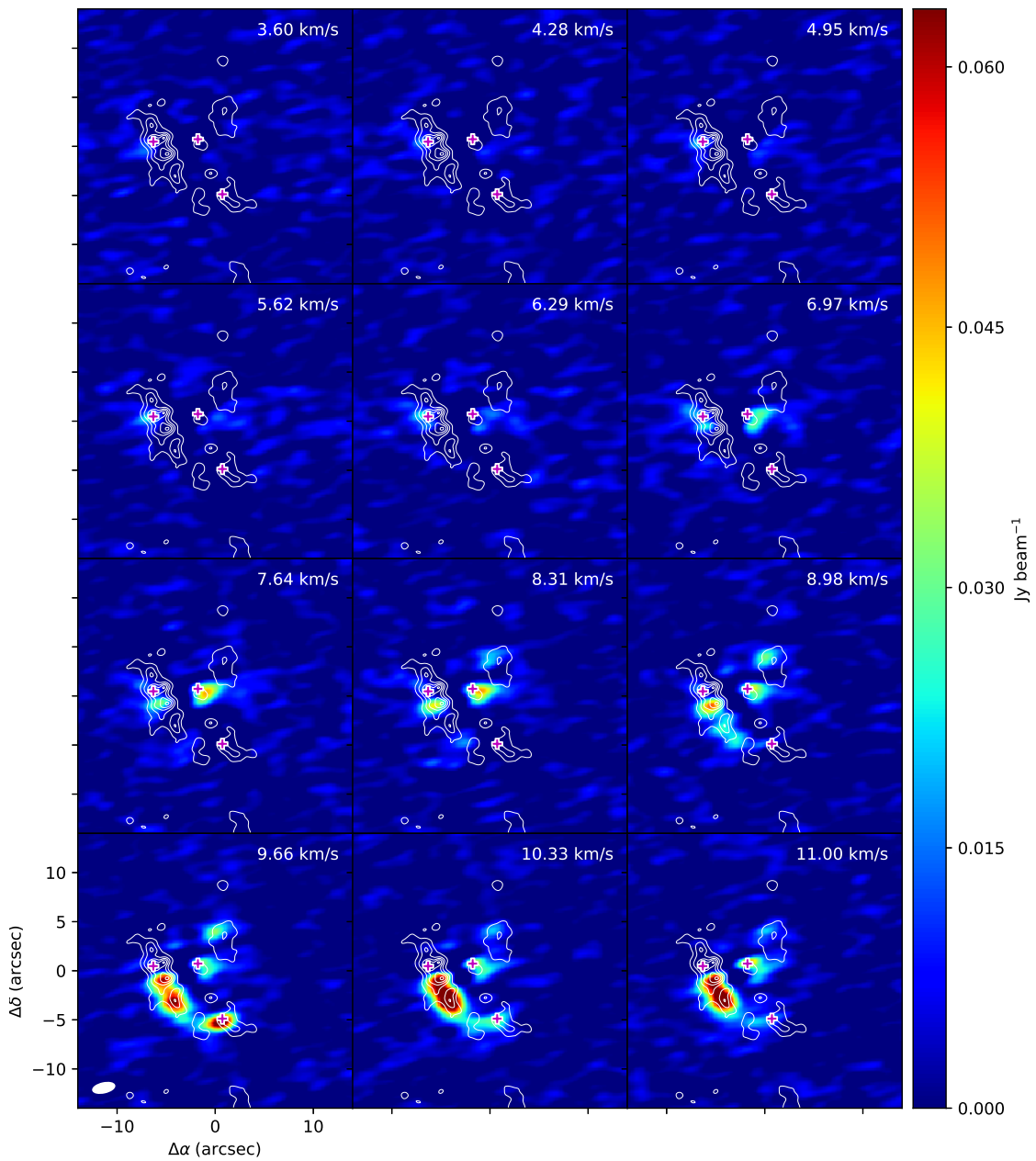


Figure B.18: 217.670 GHz

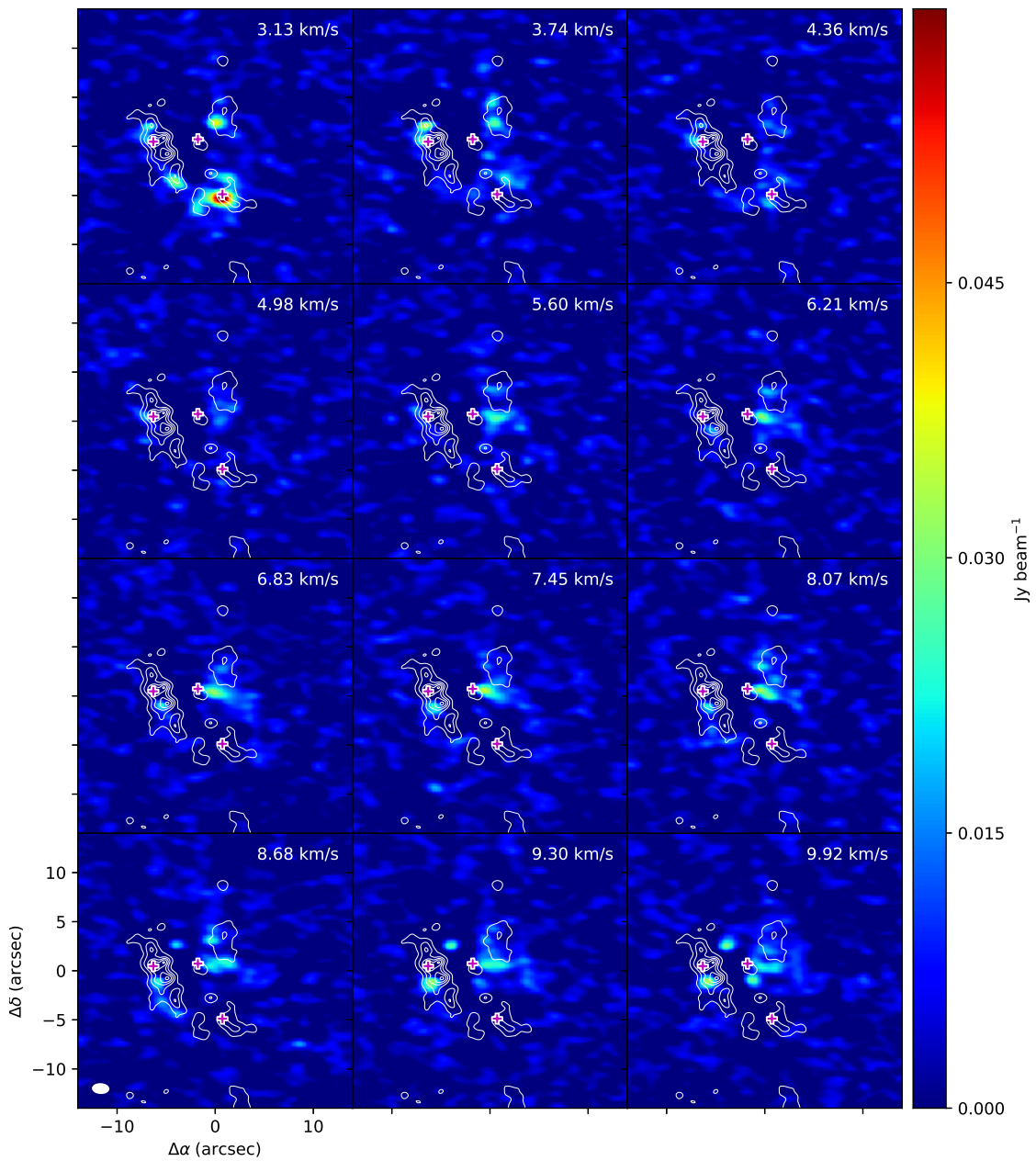


Figure B.19: 237.144 GHz

Acknowledgments

This work would have been never completed if any one of greatest persons and colleagues mentioned below is missing.

I would like to express my gratitude my supervisor, Associate Professor Hideko Nomura, for her great directions, fruitful discussions, and persistent encouragement. I would like to do the same to Dr. Tomoya Hirota and Dr. Masatoshi Oh'ishi, who led me to the field of radio astronomy. As for the data analysis of the ALMA telescope, Dr. Yoko Oya, Dr. Toshiki Saito and Dr. Ryohei Kawabe gave me elaborate guidance. I also received generous warm support and comments from Dr. Taiki Suzuki, Seongjoong Kim, and Wei Chen-en.

Finally, I am grateful to all of the colleagues of planetary groups at Tokyo Tech, and the seminar mates of ALMA interferometer seminar at National Astronomical Observatory of Japan (NAOJ) for scientific discussion and enjoyable life.

References

- Agúndez, M., Marcelino, N., & Cernicharo, J. 2018, *The Astrophysical Journal Letters*, 861, L22
- Altwegg, K., et al. 2016, *Science Advances*, 2, e1600285
- . 2017, *Monthly Notices of the Royal Astronomical Society*, 469, S130
- Blake, G. A., Sutton, E. C., Masson, C. R., & Phillips, T. G. 1987, *The Astrophysical Journal*, 315, 621
- Blake, G. A., van Dishoeck, E. F., Jansen, D. J., Groesbeck, T. D., & Mundy, L. G. 1994, *The Astrophysical Journal*, 428, 680
- Bossa, J.-B., Duvernay, F., Theulé, P., Borget, F., D'Hendecourt, L., & Chiavassa, T. 2009, *Astronomy & Astrophysics*, 506, 601
- Cazaux, S., Tielens, A. G. G. M., Ceccarelli, C., Castets, A., Wakelam, V., Caux, E., Parise, B., & Teyssier, D. 2003, *The Astrophysical Journal Letters*, 593, L51
- Chapman, N. L., et al. 2013, *The Astrophysical Journal*, 770, 151
- Ehrenfreund, P., Bernstein, M. P., Dworkin, J. P., Sandford, S. A., & Allamandola, L. J. 2001, *The Astrophysical Journal Letters*, 550, L95
- Elsila, J. E., Glavin, D. P., & Dworkin, J. P. 2009, *Meteoritics and Planetary Science*, 44, 1323

- Engel, M. H., & Nagy, B. 1982, *Nature*, 296, 837
- Favre, C., Despois, D., Brouillet, N., Baudry, A., Combes, F., Guélin, M., Wootten, A., & Wlodarczak, G. 2011, *Astronomy & Astrophysics*, 532, A32
- Feng, S., Beuther, H., Henning, T., Semenov, D., Palau, A., & Mills, E. A. C. 2015, *Astronomy & Astrophysics*, 581, A71
- Fourikis, N., Takagi, K., & Morimoto, M. 1974, *The Astrophysical Journal Letters*, 191, L139
- Fuller, G. A., Lada, E. A., Masson, C. R., & Myers, P. C. 1995, *The Astrophysical Journal*, 453, 754
- Glavin, D. P., Dworkin, J. P., & Sandford, S. A. 2008, *Meteoritics and Planetary Science*, 43, 399
- Gong, Y., et al. 2015, *Astronomy & Astrophysics*, 581, A48
- Halfen, D. T., Ilyushin, V. V., & Ziurys, L. M. 2013, *The Astrophysical Journal*, 767, 66
- Hirota, T., Kim, M. K., Kurono, Y., & Honma, M. 2015, *The Astrophysical Journal*, 801, 82
- Hirota, T., Ohishi, M., & Yamamoto, S. 2009, *The Astrophysical Journal*, 699, 585
- Hirota, T., Sakai, N., & Yamamoto, S. 2010, *The Astrophysical Journal*, 720, 1370
- Holtom, P. D., Bennett, C. J., Osamura, Y., Mason, N. J., & Kaiser, R. I. 2005, *The Astrophysical Journal*, 626, 940
- Jones, P. A., Cunningham, M. R., Godfrey, P. D., & Cragg, D. M. 2007, *Monthly Notices of the Royal Astronomical Society*, 374, 579
- Jørgensen, J. K., Schöier, F. L., & van Dishoeck, E. F. 2002, *Astronomy & Astrophysics*, 389, 908

- Jørgensen, J. K., et al. 2016, *Astronomy & Astrophysics*, 595, A117
- Kahane, C., Ceccarelli, C., Faure, A., & Caux, E. 2013, *The Astrophysical Journal Letters*, 763, L38
- Kaifu, N., Morimoto, M., Nagane, K., Akabane, K., Iguchi, T., & Takagi, K. 1974, *The Astrophysical Journal Letters*, 191, L135
- Kim, M. K., et al. 2008, *PASJ*, 60, 991
- Kleinmann, D. E., & Low, F. J. 1967, *The Astrophysical Journal Letters*, 149, L1
- Kuan, Y.-J., Charnley, S. B., Huang, H.-C., Tseng, W.-L., & Kisiel, Z. 2003, *The Astrophysical Journal*, 593, 848
- Lee, C.-W., Kim, J.-K., Moon, E.-S., Minh, Y. C., & Kang, H. 2009, *The Astrophysical Journal*, 697, 428
- Ligterink, N. F. W., et al. 2018, *Astronomy & Astrophysics*, 619, A28
- Loinard, L., Torres, R. M., Mioduszewski, A. J., & Rodríguez, L. F. 2008, *The Astrophysical Journal Letters*, 675, L29
- Marcelino, N., Agúndez, M., Cernicharo, J., Roueff, E., & Tafalla, M. 2018, *Astronomy & Astrophysics*, 612, L10
- McMullin, J. P., Waters, B., Schiebel, D., Young, W., & Golap, K. 2007, in *Astronomical Society of the Pacific Conference Series*, Vol. 376, *Astronomical Data Analysis Software and Systems XVI*, ed. R. A. Shaw, F. Hill, & D. J. Bell, 127
- Motiyenko, R. A., Ilyushin, V. V., Drouin, B. J., Yu, S., & Margulès, L. 2014, *Astronomy & Astrophysics*, 563, A137
- Oya, Y., Sakai, N., López-Sepulcre, A., Watanabe, Y., Ceccarelli, C., Lefloch, B., Favre, C., & Yamamoto, S. 2016, *The Astrophysical Journal*, 824, 88

- Oya, Y., Sakai, N., Watanabe, Y., López-Sepulcre, A., Ceccarelli, C., Lefloch, B., & Yamamoto, S. 2018, *The Astrophysical Journal*, 863, 72
- Oya, Y., et al. 2017, *The Astrophysical Journal*, 837, 174
- Pagani, L., Favre, C., Goldsmith, P. F., Bergin, E. A., Snell, R., & Melnick, G. 2017, *Astronomy & Astrophysics*, 604, A32
- Persson, M. V., et al. 2018, *Astronomy & Astrophysics*, 610, A54
- Rice, E. L., Prato, L., & McLean, I. S. 2006, *The Astrophysical Journal*, 647, 432
- Sanchez-Monge, A., Schilke, P., Ginsburg, A., Cesaroni, R., & Schmiedeke, A. 2017, STATCONT: Statistical continuum level determination method for line-rich sources, *Astrophysics Source Code Library*
- Turner, B. E. 1991, *The Astrophysical Journal Supplement*, 76, 617
- van Dishoeck, E. F., Blake, G. A., Jansen, D. J., & Groesbeck, T. D. 1995, *The Astrophysical Journal*, 447, 760
- Zapata, L. A., Schmid-Burgk, J., & Menten, K. M. 2011, *Astronomy & Astrophysics*, 529, A24